# Bone structure characterisation using neutron scattering techniques

Törnquist, Elin

2021

*Document Version:*
Publisher's PDF, also known as Version of record

# Bone structure characterisation using neutron scattering techniques

Elin Törnquist

LUND
UNIVERSITY

DOCTORAL DISSERTATION

by due permission of the Faculty of Engineering, Lund University, Sweden.
To be defended at the lecture hall *Segerfalksalen, BMC,* A10, *Lund, Sweden.*
Friday, December 10th, 2021 at 9.00.

*Faculty opponent*
Prof. Henrik Birkedal
Aarhus University

Cover artwork by Elin Törnquist, depicting neutron (bottom) and x-ray (top) tomographic image slices of a rat tibiae with a titanium implant.

Department of Biomedical Engineering
Lund University
P.O. Box 118, SE-221 00 Lund
Sweden

ISBN 978-91-8039-100-9 (print)
ISBN 978-91-8039-099-6 (pdf)
ISRN-no: LUTEDX/TEEM-1127-SE
Report No. 5/21


Printed in November 2021 by Tryckeriet i E-huset, Lund, Sweden

**Public defence**

December 10th, 2021, 9.00 in Segerfalksalen
BMC A1005, Lund University, Sölvegatan 17, 223 63 Lund, Sweden

**Supervisors**

Prof. Hanna Isaksson
*Department of Biomedical Engineering*
*Lund University, Lund, Sweden*

Associate Prof. Stephen A. Hall
*Department of Construction Sciences*
*Lund University, Lund, Sweden*

Prof. Ulf Olsson
*Department of Physical Chemistry*
*Lund University, Lund, Sweden*

**Faculty opponent**

Prof. Henrik Birkedal
*Department of Chemistry*
*Aarhus University, Aarhus, Denmark*

**Board of examination**

Prof. Ann Wennerberg
*Department of Oral Prosthodontics*
*University of Gothenburg, Sweden*

Dr. Ann Terry
*MAX IV, Sweden*

Dr. Anna Fedrigo
*ISIS Neutron and Muon Source, UK*

Deputy member: Associate Prof. Jesper Wallentin
*Department of Physics*
*Lund University, Lund, Sweden*

Deputy member: Prof. Marie Skepö
*Department of Chemistry*
*Lund University, Lund, Sweden*

| | |
|---|---|
| **Organization**<br>LUND UNIVERSITY<br>Department of Biomedical Engineering<br>Box 118, 211 00 Lund, Sweden | **Document name**<br>DOCTORAL DISSERTATION<br>**Date of issue**<br>December 10, 2021 |
| Author: Elin Törnquist | Sponsoring organization |

**Title:**Bone structure characterisation using neutron scattering techniques



**Abstract**

Bones have unique mechanical properties that originate from their main constituents: mineral, in the form of hydroxyapatite (HAp) crystals, and collagen type-I. The stiffness of the HAp mineral combined with the flexibility of collagen, and their intricate hierarchical arrangement from the smallest individual building blocks to the organ level, result in a composite tissue with a remarkable ability to withstand complex loading scenarios. The mechanisms behind this fracture resistance are not fully understood, and further insights are necessary to better comprehend the complex interplay between the constituents of bone and their multiscale structural organisation. With such knowledge, improved treatments for injuries and diseases could be developed.

X-ray based techniques have long been state-of-the-art when studying bone tissue. This is due to the strong interaction between x-rays and the heavier elements in the mineral compared to lighter elements in the surrounding tissue. However, this strong interaction overshadows the information from the collagen phase. Neutrons interact differently with matter than x-rays and exhibit an especially strong interaction with hydrogen. As hydrogen is abundant in the organic phase in bone, neutron techniques lend themselves as alternatives or complements to their x-ray counterparts for focusing on the collagen rather than the mineral phase.

The work presented in this thesis explores the potential of neutron scattering techniques in bone research and elucidates the complementary nature of neutron and x-ray scattering techniques toward the structural characterisation of bone tissue, both on the nano- and microscale. Central to the work are dual modality, i.e., neutron and x-ray, small-angle scattering (SAS) and tomography measurements on the same specimens, allowing comparisons between the two probes.

The first two studies in this thesis employed SAS to study the mineralisation process of newly formed bone, and to elucidate the possibility of gaining additional information about bone nanostructure by using neutrons. Small-angle x-ray scattering (SAXS) data from cortical bone taken from rabbits at different stages of maturation (from newborn to 6 months of age) showed an increase in thickness and orientational homogeneity of the mineral particles as the tissue matured. Comparison of the SAXS results with mechanical data from the same cohort of specimens suggested that changes in mechanical properties are explained by the amount of mineral in the tissue as well as by the dimensions of the mineral particles. Small-angle neutron scattering (SANS) and SAXS were then used to examine the nanostructure of cortical bone from larger animals of different species (cow, pig, and sheep). Comparison of the collected data showcased how neutrons and x-rays scatter in a very similar way when interacting with the bone nanostructure, suggesting that bone can be considered as a two-component composite material at the investigated length scale.

The final two studies presented in this thesis focused on the complementarity of neutron and x-ray tomography (NT and XRT) on the microscale, and on the influence of hydration on NT image quality and the mechanical properties of bone. In the first tomographic study, rat tibiae with metallic implants were imaged with both NT and XRT. Using a dual modality image registration algorithm, the image data were compared in terms of visualised structures and the quality of the visualisation. The differences in how neutrons and x-rays interact with skeletal tissues and metallic implants were highlighted. Furthermore, the benefits of using both modalities in combination, to benefit from their complementary strengths, was demonstrated. Possible improvement of the visualisation of internal structures using NT, by regulating the hydration type ($H_2O$ or $D_2O$) and quantity in the specimens, was then addressed. Rat tibiae and trabecular bovine bone plugs were imaged at different states of hydration (hydrated, dry, and rehydrated in $D_2O$ after drying) to investigate the effects on the visualisation of structures in the NT images. The imaging was combined with mechanical testing of the bone plugs to assess the changes in mechanical properties associated with drying. The trabecular bone plugs showed that drying reduced contrast between bone and soft tissues. However, no negative effects on the mechanical properties for the chosen duration of drying were found. Imaging of the rat tibiae indicated that the contrast between bone and air was high in the dried state but decreased with increasing rehydration. When free $D_2O$ was present in the medullary canal, trabecular structures could not be resolved.

In summary, the work presented in this thesis has demonstrated bone tissue to be a two-component composite material at the nanoscale, with the inorganic mineral phase affecting the tissue's mechanical properties through both the quantity and size of the mineral particles. Furthermore, the potential of NT for gaining novel insights about bone on the tissue scale is demonstrated, which paves the way for future neutron applications within the field of musculoskeletal tissue biomechanics. Due to the hydrogen sensitivity, NT can be used to identify the distribution and amount of soft skeletal tissues within a specimen, which could yield greater information about how soft skeletal tissues change, e.g., with age or due to different medical treatments. However, further investigation regarding the state of hydration is needed to optimise the visualisation of structures in the NT images.



**Key words:** small-angle neutron scattering, small-angle x-ray scattering, tomography, implant integration, nanoscale, microscale, mechanical properties

Classification system and/or index terms (if any)

| | | |
|---|---|---|
| Supplementary bibliographical information<br>ISRN: LUTEDX/TEEM-1127-SE<br>Report No. 5/21 | | **Language:** English<br>**ISBN:** 978-91-8039-100-9 (print)<br>**ISBN:** 978-91-8039-099-6 (pdf) |
| Recipient's notes | **Number of pages:** 160<br>Security classification | Price |

# Popular science summary

Vårt skelett utsätts regelbundet för höga belastningar utan att gå sönder. En av förklaringarna är att skelettet främst består av ett hårt mineral och mer flexibla proteiner. Dessa byggstenar är organiserade i specifika strukturer som ger ben unika egenskaper. På nanoskalan är mineralet format som små plattor som fäster i ett nätverk av protein. Benets egenskaper beror på mängden mineral, var mineralplattorna sitter, och hur välorganiserat nätverket är. Dessa egenskaper ändras när skelettet bildas eller läker efter en skada, men också när vi blir äldre eller får vissa sjukdomar så som benskörhet. Benvävnad delas ofta in i två olika typer. I våra långa ben, så som lårbenet, finns ett yttre kompakt skal som kallas kortikalt ben och i ändarna finns en inre porösare struktur som kallas trabekulärt ben. Dessa benstrukturer förändras också när ben bildas, läker, blir äldre eller sjukt. För att hjälpa ben att läka, eller kunna motverka att benet blir skörare, är det viktigt att förstå vilka förändringar som sker och hur dessa påverkar benets egenskaper.

Röntgenstrålning används ofta för att undersöka ben både för medicinsk diagnostik och i forskning. Röntgenstrålning som färdas genom ett material interagerar med elektronerna i materialets atomer. Ju fler elektroner desto tydligare syns strukturen som avbildas. Mineral har fler elektroner än protein och därför syns skelett tydligt medan mjuk vävnad är nästintill transparent. Röntgen är alltså inte optimalt för att undersöka proteinet i benet. I den här doktorsavhandlingen användes neutroner som komplement till röntgen. Till skillnad från röntgenljus som interagerar med elektroner så interagerar neutronerna med själva atomkärnan. Det innebär bland annat att neutroner kan skilja mellan isotoper, alltså olika varianter av samma ämne. Ett sådant exempel är väte och deuterium (tungt väte). Att få fram neutroner är svårt och därför används speciella neutronkällor. Dessutom bildas en del farliga partiklar när neutronen interagerar med atomer vilket gör att neutroner endast kan användas på prover och inte på patienter. Neutroner interagerar väldigt starkt med väte, vilket det finns gott om i protein. Målet med den här avhandlingen var att undersöka hur neutronmetoder kan vara behjälpliga i benforskning. Utifall att neutroner kan se saker som inte syns med röntgen, skulle metoderna kunna assistera i utveckling av bättre metoder för att hjälpa ben läka efter en fraktur eller sjukdom.

I de två första studierna i avhandlingen användes en teknik som kallas låg-vinkel-spridning för att titta på benets struktur på nanoskalan. Genom att belysa ett benprov med en röntgen- eller neutronstråle fås ett spridningsmönster när strålen interagerar med mineralplattorna och proteinnätverket. Spridningsmönstret från

röntgen kommer till största delen från mineralet och signalen från proteinet överskuggas så att den inte är enkelt att titta på. I den första studien användes röntgenspridning för att undersöka hur mineralet förändras med ökad ålder i benbitar från kaniner. Resultatet visade att mineralplattorna var tjockare och mer välorganiserade ju äldre benvävnaden var, och att inte bara mängden mineral påverkar benvävnadens egenskaper utan också tjockleken på mineralplattorna. I nästa studie användes både röntgen och neutroner för att titta på benbitar från ko, gris och får. Jämförelse av spridningsmönstren visade att neutroner och röntgen sprids på samma sätt. Det innebär att de enda strukturerna som påverkar spridningsmönstret är mineralet och proteinet, vilket har betydelse för hur mönstret ska tolkas och vilka slutsatser som kan dras gällande benstrukturen.

I de följande två studierna användes datortomografi för att titta på benets mikrostruktur. Med tomografi tas många två-dimensionella bilder på olika positioner kring benet, och dessa sätts sedan samman till en tre-dimensionell bild. Fördelen med tomografi är att man mer exakt kan se var till exempel ett implantat är placerat. Att titta på just benimplantat är viktigt för att förstå varför de ibland lossnar från benet. Vanligtvis är benimplantat gjorda i metall och det är svårt att titta på benvävnaden nära implantatet med röntgen eftersom bildartifakter skapas när röntgenstrålen interagerar med metallen. Neutroner interagerar inte på samma sätt med metall så med neutrontomografi kan man tydligt se benet precis intill implantatet. I den tredje studien användes neutron- och röntgentomografibilder av råttben med implantat av titan. Förutom att benet nära implantatet syntes bättre i neutronbilderna sågs även mjuk skelettvävnad, vilket inte syns tydligt i röntgenbilder. En utmaning med neutrontomografi är dock att neutroner interagerar starkt med väte. Väte finns inte bara i proteinnätverket utan också i vatten. Kroppens vattenhalt gör att neutrontomografibilder av blöta benprover visar sämre kontrast mellan ben och bakgrund än röntgenbilder. Samtidigt är det viktigt att bibehålla samma vätskehalt som i kroppen eftersom benets egenskaper påverkas av dess vattenhalt. I den sista studien jämfördes neutrontomografibilder av torrt och blött ben. Vattnet byttes mot tungt vatten genom torkning och rehydrering, i ett försök att förbättra kontrasten mellan vävnad och vätska, eftersom deuteriumet i tungt vatten inte interagerar lika starkt med neutroner som vätet i benet. Mekaniska tester användes för att se hur benets mekaniska egenskaper påverkades. Resultatet visade att kontrasten mellan tungt vatten och ben var låg, men att benets egenskaper inte verkade påverkas av torkningen.

Sammanfattningsvis demonstrerar studierna i den här doktorsavhandlingen att neutrontekniker har potential att användas för benforskning och att informationen som fås komplimenterar den från röntgentekniker. Mer specifikt har studierna visat att benvävnad huvudsakligen består av mineralplattor i ett proteinnätverk på nanonivå, och att mineralplattorna blir tjockare och mer välorganiserade ju äldre benet blir. De visar också att neutrontomografi är en lovande teknik för att titta både på benvävnad nära metallimplantat och på mjuk skelettvävnad. Dock behövs fler studier kring balans av vätskehalten så att benets egenskaper bibehålls samtidigt som neutronbilderna har god kontrast.

# Abstract

Bones have unique mechanical properties that originate from their main constituents: mineral, in the form of hydroxyapatite (HAp) crystals, and collagen type-I. The stiffness of the HAp mineral combined with the flexibility of collagen, and their intricate hierarchical arrangement from the smallest individual building blocks to the organ level, result in a composite tissue with a remarkable ability to withstand complex loading scenarios. The mechanisms behind this fracture resistance are not fully understood, and further insights are necessary to better comprehend the complex interplay between the constituents of bone and their multiscale structural organisation. With such knowledge, improved treatments for injuries and diseases could be developed.

X-ray based techniques have long been state-of-the-art when studying bone tissue. This is due to the strong interaction between x-rays and the heavier elements in the mineral compared to lighter elements in the surrounding tissue. However, this strong interaction overshadows the information from the collagen phase. Neutrons interact differently with matter than x-rays and exhibit an especially strong interaction with hydrogen. As hydrogen is abundant in the organic phase in bone, neutron techniques lend themselves as alternatives or complements to their x-ray counterparts for focusing on the collagen rather than the mineral phase.

The work presented in this thesis explores the potential of neutron scattering techniques in bone research and elucidates the complementary nature of neutron and x-ray scattering techniques toward the structural characterisation of bone tissue, both on the nano- and microscale. Central to the work are dual modality, i.e., neutron and x-ray, small-angle scattering (SAS) and tomography measurements on the same specimens, allowing comparisons between the two probes.

The first two studies in this thesis employed SAS to study the mineralisation process of newly formed bone, and to elucidate the possibility of gaining additional information about bone nanostructure by using neutrons. Small-angle x-ray scattering (SAXS) data from cortical bone taken from rabbits at different stages of maturation (from newborn to 6 months of age) showed an increase in thickness and orientational homogeneity of the mineral particles as the tissue matured. Comparison of the SAXS results with mechanical data from the same cohort of specimens suggested that changes in mechanical properties are explained by the amount of mineral in the tissue as well as by the dimensions of

the mineral particles. Small-angle neutron scattering (SANS) and SAXS were then used to examine the nanostructure of cortical bone from larger animals of different species (cow, pig, and sheep). Comparison of the collected data showcased how neutrons and x-rays scatter in a very similar way when interacting with the bone nanostructure, suggesting that bone can be considered as a two-component composite material at the investigated length scale.

The final two studies presented in this thesis focused on the complementarity of neutron and x-ray tomography (NT and XRT) on the microscale, and on the influence of hydration on NT image quality and the mechanical properties of bone. In the first tomographic study, rat tibiae with metallic implants were imaged with both NT and XRT. Using a dual modality image registration algorithm, the image data were compared in terms of visualised structures and the quality of the visualisation. The differences in how neutrons and x-rays interact with skeletal tissues and metallic implants were highlighted. Furthermore, the benefits of using both modalities in combination, to benefit from their complementary strengths, was demonstrated. Possible improvement of the visualisation of internal structures using NT, by regulating the hydration type ($H_2O$ or $D_2O$) and quantity in the specimens, was then addressed. Rat tibiae and trabecular bovine bone plugs were imaged at different states of hydration (hydrated, dry, and rehydrated in $D_2O$ after drying) to investigate the effects on the visualisation of structures in the NT images. The imaging was combined with mechanical testing of the bone plugs to assess the changes in mechanical properties associated with drying. The trabecular bone plugs showed that drying reduced contrast between bone and soft tissues. However, no negative effects on the mechanical properties for the chosen duration of drying were found. Imaging of the rat tibiae indicated that the contrast between bone and air was high in the dried state but decreased with increasing rehydration. When free $D_2O$ was present in the medullary canal, trabecular structures could not be resolved.

In summary, the work presented in this thesis has demonstrated bone tissue to be a two-component composite material at the nanoscale, with the inorganic mineral phase affecting the tissue's mechanical properties through both the quantity and size of the mineral particles. Furthermore, the potential of NT for gaining novel insights about bone on the tissue scale is demonstrated, which paves the way for future neutron applications within the field of musculoskeletal tissue biomechanics. Due to the hydrogen sensitivity, NT can be used to identify the distribution and amount of soft skeletal tissues within a specimen, which could yield greater information about how soft skeletal tissues change, e.g., with age or due to different medical treatments. However, further investigation regarding the state of hydration is needed to optimise the visualisation of structures in the NT images.

# List of appended papers

This thesis consists of a review of the author's work in the field of biomedical engineering. The following selection of the author's publications is referred to in the text by their Roman numerals. Papers I-IV are appended at the end of the thesis and have been reproduced with the permission of the copyright holders.

I. **Törnquist, E.**, Isaksson, H., Turunen, M. J. Mineralization of cortical bone during maturation and growth in rabbits. *Journal of Bone and Mineral Metabolism (2020)*. 38:289-298. 10.1007/s00774-019-01068-y

II. **Törnquist, E.**, Gentile, L., Prévost, S., Diaz, A., Olsson, U., Isaksson, H. Comparison of small-angle neutron and x-ray scattering for studying cortical bone nanostructure. *Scientific Reports (2020)*. 10:14552. 10.1038/s41598-020-71190-9

III. **Törnquist, E.**, Le Cann, S., Tudisco, E., Tengattini, A., Andò, E., Lenoir, N., Hektor, J., Raina, D. B., Tägil, M., Hall, S. A., Isaksson, H. Dual modality neutron and x-ray tomography for enhanced image analysis of the bone-metal interface. *Physics in Medicine & Biology (2021)*. 66:135016. http://doi.org/10.1088/1361-6560/ac02d4

IV. **Törnquist, E.**, Le Cann, S., Tengattini, A., Helfen, L., Kok, J., Hall, S. A., Isaksson, H. Hydration state affects neutron tomographic images of bone. *Manuscript*

For all papers, the author of this thesis planned the study together with the co-authors, prepared specimens, carried out the experiments, analysed and interpreted the data, and drafted the manuscripts.

# Acknowledgements

This journey has been an amazing experience in so many ways, one of them being that I have had the pleasure of working with so many wonderful people.

I want to start with thanking my main supervisor, Hanna, for giving me this opportunity and for guiding me through this thesis work. Your zealousness, work ethics, and high standards have always impressed and inspired me. You have been a great mentor, and you have helped me grow both as a researcher and as a person. I would also like to thank my co-supervisors, Steve and Ulf, for guiding me through this PhD. Thank you for sharing your knowledge, for your practical help, creative ideas, and for inspiring me to look beyond my own projects.

I also want to thank my opponent, Prof. Henrik Birkedal, and the members of the examination committee, Prof. Ann Wennerberg, Dr. Ann Terry, Dr. Anna Fedrigo, Associate Prof. Jesper Wallentin, and Prof. Marie Skepö for critically reading my thesis and challenging me during my defence to ensure the quality of my work.

To all my colleagues in the biomechanics group, thank you for making these years so fun and inspiring. Thomas and Joeri, you both started and finished just before me. Making this journey together with you has been a pleasure. Anna, Lorenzo, Isabella, and Maria, thanks for all the good times both at and outside of the office. I am very lucky to have worked with such an amazing group of people. Gustavo, Hector, Tobias, and Kunal, welcome to the group. I have no doubts that you will carry the torch of amazingness onward. A big thanks to Isabella and Kunal for proofreading my thesis.

To my fellow colleagues at BMC and the E-house. Deepak and Yang, thank you for being so welcoming and such great collaborators. Johan, thank you for being a wonderful and approachable head of department. Ulrika, you are one of the kindest people I have ever met. Thank you for all your help throughout the years and for all our lovely coffee talks. Jonatan, William, and Moritz, let's continue the boardgames and beer drinking, shall we?

To all the colleagues and students that I have had the fortune of working with over the years. Sophie, your meticulousness and enthusiasm regarding research have been huge inspirations to me. I am so happy to be able to not only call you a colleague but also a close friend. Hannicka, sharing an office with you was one of the best parts of my PhD. Ornella, it was a pleasure supervising you. Mikael, I very much enjoyed working with you and having beers with you. Karin, Meral,

Lissa, and Leon, thank you for contributing to a great atmosphere at work and for all the fun times outside of work. Luigi, working with you has been almost as much fun as having cocktails with you. Ale, thank you for always going above and beyond in making sure our experiments go as well as possible, and for patiently answering all my questions about neutron imaging.

Thank you to all collaborators that have helped make the studies during my PhD possible. Sophie Le Cann, Luigi Gentile, Alessandro Tengattini, Erika Tudisco, Joeri Kok, Mikael Turunen, Deepak Raina, Edward Andò, Nicolas Lenoir, Sylvain Prévost, Ana Diaz, Johan Hektor, Magnus Tägil, Lukas Helfen, Viviane Lütz-Bueno, Mariana Verezhak, Manuel Guizar-Sicairos, Heikki J. Helminen, Anders Kaestner, Felix Tong, Vladimir Novak, Filip Lenrick, Mats Christensson, Jonas Engqvist, and Aleksandra Turkiewics. Without you this thesis would be very empty.

To Ale, Nico, and Eddy. Thank you for giving me the opportunity to come to Grenoble and work with you at 3SR and ILL. It was a great experience in so many ways.

To my Grenoblois friends. Rob, Ale, Angela, Cyrille, Olga, Bratislav, and Sonja, thank you for welcoming me into your group and making my time in Grenoble so much fun. Ilija, thanks for all the stupid memes, they made covid confinement more bearable.

To SwedNess. Being part of this graduate school has been very valuable. It has provided me with so many opportunities and opened so many doors. To my fellow neutron scatterers, it has been great fun exploring neutron facilities and spa hotels with you. Karolina, I have greatly enjoyed our fancy lunch dates and running with you, and I hope we will continue with both. Karolina and Filippa, I'm deadly serious about our graduation trip to Tartu so that we can end our PhD journeys the same way they started, with cocktails at Willy & Rudy!

To Malmö Shitty Släckers. Thanks for all the Midsummer and New Year's celebrations, parties, beach BBQs, beer drinking, etc. Bella, thanks for being an awesome hiking partner and such a reliable source of wine. Erik, occasionally punching you at Thai boxing has been a great stress relief.

To Rob. Thank you for your input and support, but most of all for helping me put things in perspective and for getting me to focus on other things than just work.

To Chris. Thank you for being a great friend. Your support, encouragement, and blatant honesty have been invaluable to me.

Finally, and most importantly, to my family. Mamma, Maria, och Björn. Tack för att ni alltid finns där och stöttar mig, vad det än gäller. Utan er hade inget av det här varit möjligt.

# List of abbreviations

| | |
|---|---|
| **2D** | Two-dimensional |
| **3D** | Three-dimensional |
| **AUC/TA** | Area under curve / Total area |
| **BV/TV** | Bone volume / Total volume (bone volume fraction) |
| **CNR** | Contrast-to-noise ratio |
| **Ctrl** | Control |
| **$D_2O$** | Deuterium dioxide (heavy water) |
| **DECT** | Dual energy computed tomography |
| **DVC** | Digital volume correlation |
| **eV** | electron volt |
| **FOV** | Field of view |
| **FWHM** | Full width at half maximum |
| **FTIR** | Fourier transform infrared spectroscopy |
| **HAp** | Hydroxyapatite |
| **$H_2O$** | Hydrogen dioxide (normal water) |
| **LINAC** | Linear accelerator |
| **kV** | Kilovolt ($10^3$ volt) |
| **µA** | Microampere ($10^{-6}$ ampere) |
| **µm** | Micrometre ($10^{-6}$ m) |
| **ND** | Neutron diffraction |
| **nm** | Nanometre ($10^{-9}$ m) |
| **NT** | Neutron tomography |
| **ROI** | Region of interest |
| **SANS** | Small-angle neutron scattering |
| **SAS** | Small-angle scattering |
| **SAXS** | Small-angle x-ray scattering |
| **SDD** | Sample to detector distance |
| **SLD** | Scattering length density |
| **SNR** | Signal-to-noise ratio |
| **TMD** | Tissue mineral density |
| **TOF** | Time-of-flight |
| **Trtd** | Treated |
| **XRF** | X-ray fluorescence |
| **XRT** | X-ray tomography |
| **Å** | Ångström ($10^{-10}$ m) |

# Table of Contents

**Popular science summary** ..... **vii**

**Abstract** ..... **ix**

**List of appended papers** ..... **xi**

**Acknowledgements** ..... **xii**

**List of abbreviations** ..... **xiv**

**Table of Contents** ..... **xv**

**1. Introduction** ..... **1**

**2. Aim and design of the study** ..... **3**

2.1 Design of the study ..... 4

**3. Background** ..... **5**

3.1 Bone ..... 5

3.2 Neutron and x-ray techniques for structural characterisation ..... 7

*Interaction with matter* ..... *7*

*Neutron and x-ray sources* ..... *8*

*Small-angle scattering* ..... *11*

*Theory* ..... *11*

*SAS for bone research* ..... *12*

*Tomographic imaging* ..... *15*

*Theory* ..... *15*

*Image artefacts* ..... *16*

*Tomographic imaging in bone research* ..... *17*

3.3 Mechanical testing ..... 18

**4. Material & Methods** ..... **21**

4.1 Samples ..... 21

*Cortical bone from rabbits (Study I)* ..... *21*

*Cortical bone from cow, sheep, and pig (Study II)* ..... *21*

*Rat tibiae with metal implants (Study III)* ..... *22*

*Rat tibiae and trabecular bovine bone plugs (Study IV)* ..... *22*

4.2 Small-angle scattering (Studies I-II) ..... 24

*SAXS for studying mineralisation in cortical bone (Study I)* ..... *24*

*SANS and SAXS from cortical bone for nanostructure characterisation (Study II)* ..... *24*
4.3 Tomographic imaging (Studies I-IV) ..... 25
*XRT for tissue mineral density assessment (Study I)* ..... *25*
*XRT for structural characterisation of cortical bone (Study II)* ..... *26*
*NT and XRT of rat tibiae with metal implants (Study III)* ..... *26*
*Effects of hydration state on NT images of bone (Study IV)* ..... *26*
4.4 Mechanical testing (Study IV) ..... 27
*Effects of hydration state on mechanical properties of bone (study IV)* ..... *27*
4.5 Data analysis ..... 28
*Small-angle scattering (Studies I-II)* ..... *28*
*SAXS for studying mineralisation in cortical bone (Study I)* ..... *28*
*SANS and SAXS for structural characterisation of cortical bone (Study II)* ..... *28*
*Tomographic imaging (Studies I-IV)* ..... *30*
*Tissue mineral density calculation (Studies I-II)* ..... *30*
*Microstructural orientation (Study II)* ..... *30*
*Bimodal image registration and joint histogram analysis (Study III)* ..... *30*
*Volume fraction calculation (Studies III-IV)* ..... *32*
*Image quality assessment (Studies III- IV)* ..... *32*
*Statistical analysis (Studies I, III, and IV)* ..... *33*

**5. Results ..... 34**

5.1 Mineralisation during maturation and growth (Study I) ..... 34
5.2 Comparison of SANS and SAXS (Study II) ..... 36
5.3 Comparison of NT and XRT for visualising skeletal tissues (Study III) ..... 38
5.4 Effects of hydration state on NT images of bone (Study IV) ..... 40

**6. Discussion ..... 43**

6.1 General ..... 43
6.2 Small-angle scattering ..... 44
6.3 Tomographic imaging ..... 47
6.4 Future perspectives ..... 49

**7. Summary and conclusions ..... 51**

**8. References ..... 53**

**9. Appended papers ..... 67**

# 1. Introduction

Bone is a complex tissue composed primarily of an inorganic mineral phase, an organic collagen type-I phase, and water [1,2]. The organic phase is organised as a matrix in which the mineral particles are interwoven. The stiffness of the mineral in combination with the flexibility of the collagen, and their intricate hierarchical arrangement from individual building blocks up to the organ level, result in a composite tissue with unique mechanical properties optimised toward fracture resistance [2–4]. However, the mechanisms behind this fracture resistance are yet to be fully identified. Changes in the composition and structure of bone occur during maturation and growth [5–9], and also as a result of degenerative disorders such as osteoporosis [10]. How these changes relate to the mechanical properties of bone is still under investigation. To fully elucidate the contribution from each constituent and their complex hierarchical organisation, all length scales need to be investigated as they all contribute to the macroscopic mechanical behaviour of bone tissue [11].

The presence of the mineral phase in bone and the associated strong interaction between x-rays and the heavier elements in the mineral, compared to the lighter elements in the collagen matrix, have led to the emergence of x-ray techniques as a key tool for the study of bone tissue. The difference in x-ray interaction between the mineral and collagen phases is a direct consequence of how x-rays interact with the electron cloud of atoms, and so the greater number of electrons in the mineral leads to a stronger interaction. At the nanoscale, this means that the mineral can be distinguished within the collagen matrix by means of diffraction and SAS, allowing the size, shape, and distribution of the mineral particles to be explored. This information can be used to better understand, e.g., the mineralisation process during maturation and growth of bone tissue, how different loading scenarios affect the distribution and amount of mineral, and changes that occur during ageing and disease. In turn, the effects of these changes on the mechanical stability of the tissue can be identified by combining the structural characterisation with mechanical testing. However, the strong interaction between x-rays and mineral results in difficulties in studying the collagen phase, as its scattering signal is partially overshadowed by that of the mineral. At the macro- and microscale, this higher interaction with the mineral results in good x-ray contrast between bone and surrounding non-mineralised tissues, which is exploited, e.g., in x-ray radiography and tomography to diagnose orthopaedic conditions. However, when metallic objects such as implants are

present, the large difference in attenuation between metal and bone can result in image artefacts that make analysis of peri-implant bone challenging.

As opposed to x-rays, neutrons interact with the atomic nuclei, as their lack of electrical charge allows them to pass through the electron cloud. This interaction does not follow as simple of a pattern as x-rays, where an increase in the number of electrons equates to a stronger interaction. Instead, the interaction between neutrons and atoms follows a seemingly disorganised pattern. One of the largest neutron interactions (neutron cross section) is with hydrogen, making neutrons an ideal probe for detecting variations in hydrogen concentration. As hydrogen is a dominant component in biological tissue, neutron scattering techniques can be used to study both structure and composition in biological samples.

Applications of neutron techniques for structural characterisation in bone research are still limited. At the time of writing this thesis, a Scopus search for journal and review articles where the title, abstract, or key words contain the words "bone tissue structure" and "x-rays" or "bone tissue structure" and "ct" yielded 8,693 results whilst a search for "bone tissue structure" and "neutrons" yielded 41 results. It should be noted that these search terms were not exact enough to exclude some studies of, e.g., soft tissues, and most likely missed some publications. Nevertheless, there is a staggering difference in the number of publications employing neutron techniques compared to x-ray techniques in bone research. Most previous neutron studies have employed diffraction to study bone at the nanoscale. These studies aimed at, e.g., gaining insight into the HAp mineral plates in terms of size [12–14], and orientation close to implants [15–17], as well as to study the collagen matrix in terms of molecular spacing in bone [18–20] and in mineralised and non-mineralised tendon tissue [21,22]. In the aforementioned studies, neutrons were chosen over x-rays due principally to their penetrating power, a factor that allows for larger specimens to be used, and because of the reduced influence of the mineral on the acquired data. SAS probes slightly larger lengths scales than diffraction. SAXS has been used extensively (> 300 articles) to gain insight into the mineral phase in bone. Searching Scopus for articles where SANS was used for bone tissue characterisation yields only two results (the author is aware of one additional SANS study that did not appear in the search), one of which is the second study presented in this thesis. For structural characterisation at the microscale, XRT is state-of-the-art. To the best of the author's knowledge, apart from emerging applications in palaeontology, the only studies (4) employing NT in bone research come from the research group the author belongs to, one of the publications being the third study presented in this thesis [23–26].

In summary, the discussed literature searches indicate a limited appreciation for the potential application of neutron scattering techniques toward the structural characterisation of bone tissue. As neutrons have been found to be complementary to x-rays in many other fields of research, their potential to provide information also in bone research needs to be explored.

# 2. Aim and design of the study

The overall aim of this thesis work was to investigate the possibilities of using neutron scattering techniques as a complement or alternative to x-rays for studying bone tissue structure over different length scales. Neutrons and x-rays interact differently with materials, resulting in different contrasts for the two probes. As bone tissue contains an inorganic mineral phase, for which the interaction is large with x-rays, and an organic collagen phase, where the abundance of hydrogen results in a large interaction with neutrons, we hypothesised that the two probes could yield complementary information about bone structure. A comparison of neutron and x-ray techniques has been made considering SAS, for nanostructural characterisation, and tomography, for microstructural characterisation. Consequently, situations and conditions where neutrons could be preferable to x-rays were identified by comparing pros and cons of the respective techniques.

The aims of the individual studies were:

I. *To gain insights into nanostructural changes in the mineral phase as bone matures and grows and relate these changes to alterations both in the collagen matrix and in the mechanical properties of the tissue*.

II. *To elucidate complementarity of neutrons and x-rays for obtaining nanostructural information about the mineral and collagen components in bone.*

III. *To explore complementarity of neutron and x-ray tomography for obtaining microstructural information about hard and soft skeletal tissues.*

IV. *To identify how neutron tomographic images of bone are affected by the hydration state of the specimens and investigate how the mechanical properties can be maintained whilst simultaneously being able to visualise internal structures for microstructural characterisation.*

## 2.1 Design of the study

Figure 2.1 illustrates the specific aims of the individual studies within the design of the thesis project.

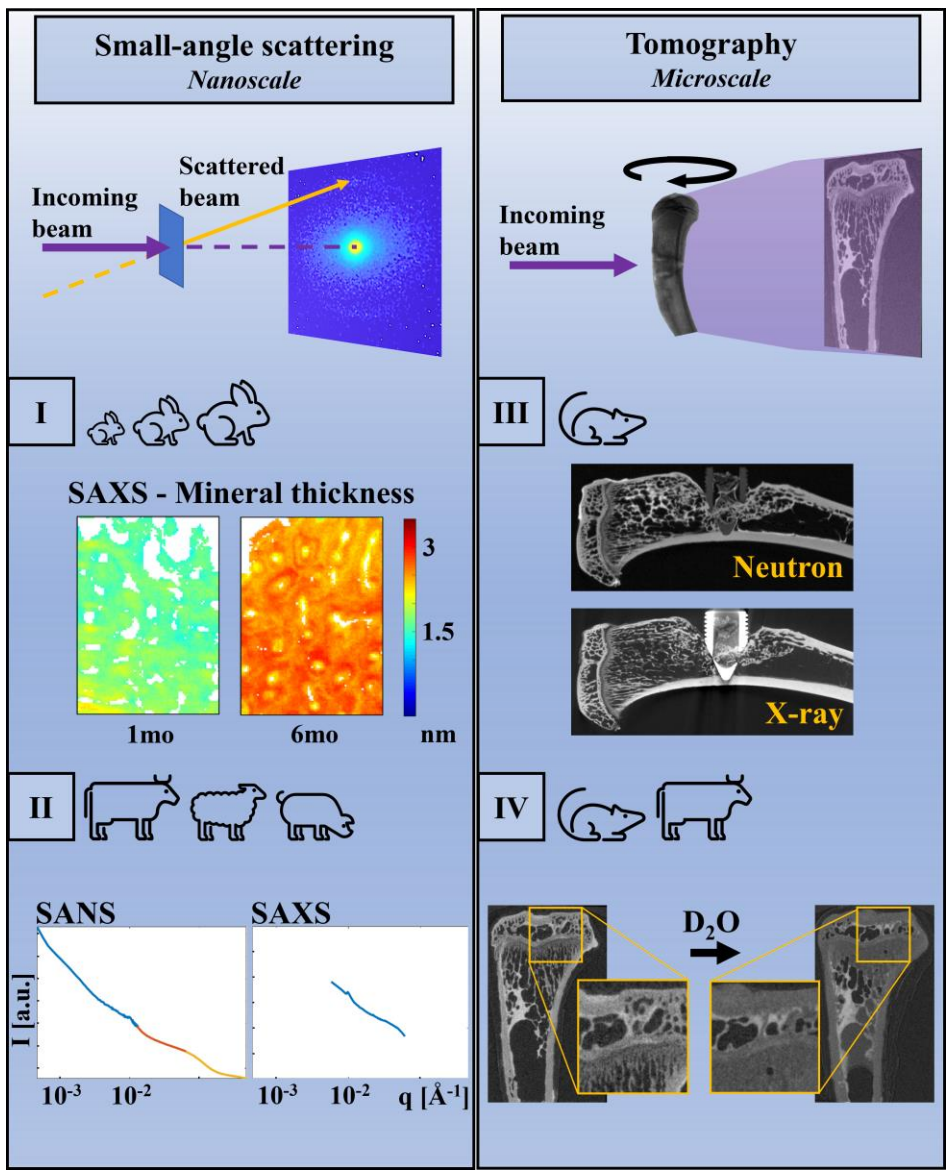


Figure 2.1. Overview of the design of the studies. The roman numerals (I-IV) refer to the aims and appended studies. The species used for obtaining the specimens are indicated for each study.

# 3. Background

## 3.1 Bone

Bone is a complex hierarchically structured tissue. It is primarily composed of an inorganic HAp mineral phase, an organic collagen type-I based matrix, water, and non-collagenous proteins [1,2,8,11,27–33]. The stiffness of the mineral in combination with the flexibility of the collagen, plus their intricate hierarchical arrangement from individual building blocks to organ level (Figure 3.1), result in a composite tissue with unique mechanical properties [2–4,34].

At the nanoscale, the mineral phase is found as elongated, slightly curved plate-shaped crystals interwoven in a collagen matrix, creating mineralised collagen fibrils [1,11,29,30,32,35]. Collagen is a triple helical molecule with diameter and length of 15 Å and 3000 Å, respectively. The molecules congregate into fibrils with an approximate diameter of 1000 Å and intrafibrillar spacing of ~100 Å. The collagen molecules in the fibrils are staggered axially such that zones of overlap and gaps form with a specific periodicity, referred to as D-spacing, of approximately 670 Å. The mineral plates nucleate both within the periodic gap zones and on the surface of the fibrils. They have a crystal c-axis aligned primarily with the main axis of the collagen fibril [7,8,28,36]. The mineral starts out as thin platelets that gradually increase in thickness. During maturation and growth, mineral amount, crystal size, and structural order increase [5–9]. In mature bone, the mineral plates have approximate lengths and widths of a few hundred Å, and thickness of 30 Å [31,37–41]. Furthermore, the amount and degree of order of the collagen matrix have been found to increase as the tissue matures [4–6,42]. Water is present in different compartments: in pores and canals (on the micrometre scale), loosely bound to the surfaces of collagen fibrils, between the collagen and mineral phases, and more tightly bound to the collagen molecule and inside the mineral crystal structure [43,44].

At the microscale, the mineralised collagen fibrils congregate into fibres. The organisation of these fibres differs with anatomical location and age of the tissue [1,11]. In woven bone, which is deposited during development and fracture repair, the fibrils have little or no preferred orientation. Woven bone is replaced by lamellar bone, where the fibrils are organised in 3-7 µm thick lamellae. Lamellar bone is the most prevalent organisational type found in mammalian bone. It makes up the two main tissue types found in all skeletal bones, namely cortical and trabecular bone. Cortical bone is found as an outer shell enclosing the

trabecular bone. The thickness of the cortical bone varies between tenths of a millimetre to several centimetres depending on species and anatomical site [11]. Cortical bone has a porosity of ~6%, mainly due to blood vessels and nerve fibres permeating the bone tissue. During cortical bone formation, circular structures form around these blood vessels and nerve fibres. These structures are known as primary osteons and are made up of concentric lamellae. As the deposition of osteon lamellae start from the periphery and continue inwards, mineralisation as a function of tissue age can be studied through the radial profiles of osteons. Osteons are typically aligned parallel with the main axis of the bone. Trabecular bone has a porosity of ~80% and is made up of a sponge-like 3D structure comprised of bone trabeculae. Each individual trabeculae has a thickness of a few hundred micrometres. In some bones, e.g., vertebrae, trabecular bone fills the entire inner volume whilst other bones, such as the epiphysis in long bones, are filled only in parts. The porosities in trabecular bone is filled with bone marrow.

Bone tissue is continuously remodelled to take care of microdamage and to optimise the structure according to the experienced mechanical loading environment. The remodelling includes resorption of old bone and formation of new bone. The balance between these is governed by the mechanical loads the tissue is exposed to [45]. Consequently, denser bone is found in regions exposed to high loads. Additionally, directional loading results in anisotropic bone structure. During cortical bone remodelling, primary osteons are substituted for secondary osteons [1,46]. The secondary osteons are approximately 100-200 µm in diameter and the enclosed canal, known as the Haversian canal, have a diameter of about 30-40 µm.

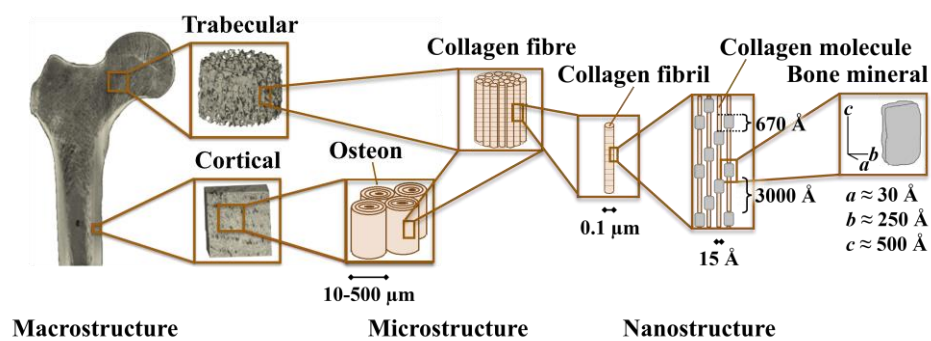


Figure 3.1. Hierarchical structure of bone. At the organ scale, a skeletal long bone consists of a cortical bone cortex enclosing trabecular bone found in the epiphysis. During formation and remodelling, osteonal structures are formed in the cortical bone. These microstructures are made up of mineralised collagen fibres. At the nanoscale, the collagen fibres are found to consist of collagen molecules congregated into fibrils in a staggered manner. Plate shaped HAp crystals exist between the fibrils and inside the gap zones in the staggered arrangement of the collagen molecules.

## 3.2 Neutron and x-ray techniques for structural characterisation

Structural characterisation of bone tissue is important for understanding how the constituents and their organisation affect the mechanical properties of bone and how this relates to the material's fracture resistance. As bone is a hierarchically organised material, all length scales need to be investigated to understand the complex interplay both between the constituents and between their different arrangements. X-ray techniques are state-of-the-art in bone research, benefitting from the strong interaction between x-rays and the mineral phase in bone. SAXS is often used to look at the arrangement of collagen and mineral at the nanoscale. However, the strong scattering signal from the mineral overshadows the signal from the collagen, making collagen characterisation challenging. XRT is a common tool to assess structures on the nano-/micro-/macroscale in 3D. As for scattering, the strong interaction between x-rays and bone mineral gives good contrast between bone and other tissues. However, soft tissues are not well captured with x-ray imaging. Additionally, image artefacts in the vicinity of metallic implants can create difficulties in visualising the peri-implant bone using XRT. Due to differences in how x-rays and neutrons interact with matter, the corresponding neutron techniques – SANS and NT – offer the potential for complementary information to their x-ray counterparts.

### Interaction with matter

As neutrons lack electrical charge, they penetrate through the electron shell of atoms and interact with the nucleus [47]. In contrast, the electromagnetic quality of x-rays causes them to interact with the negatively charged electrons. As such, the interaction probability (cross section, $\sigma$) between x-rays and matter follows a linear relationship with regard to atomic mass, whilst no such relationship exists for neutrons. The cross sections for both neutrons and x-rays include the effects of both absorption and scattering, $\sigma_{tot} = \sigma_{ab} + \sigma_{sc}$. Furthermore, $\sigma$ depends on both atomic number, $Z$, and on the energy of the radiation. Probing biological systems requires cold or thermal/epithermal neutrons (0.025 eV – 10 keV) [47–49]. In this energy range, absorption and elastic scattering are the prevalent modes of interaction with matter, whilst inelastic scattering becomes prominent at higher energies. For x-rays, the typical energy range used in bone research is 12-140 keV [50,51]. The types of interactions here are elastic scattering, photoelectric attenuation, and inelastic Compton scattering [51–53]. Photoelectric attenuation is prominent at lower energies (< 50 keV) and its probability scales with atomic number as $\propto Z^3$. Compton scattering dominates at higher energies (> 90 keV) and depends on the electron density of the material. As biological tissues have similar electron densities, Compton scattering provides little contrast information. Conversely, due to the cubic proportionality between the probability of

photoelectric absorption and atomic number, even small differences between tissues yield contrast at lower x-ray energies.

Neutrons and x-rays are highly complementary probes, as the differences in material-specific cross section provides differing contrasts between material phases (Figure 3.2). In addition, the neutron interaction with the atomic nucleus means that they are sensitive to atomic mass number and so have different cross sections for different isotopes, allowing these to be distinguished from one another. One of the largest differences in neutron isotopes cross section is that between hydrogen, H or $^{1}$H, and its stable isotope deuterium, D or $^{2}$H (Figure 3.2). As hydrogen is naturally abundant in organic compounds, contrast between different compounds can be low. In neutron scattering studies of organic compounds such as proteins, the difference in interaction probability between hydrogen and deuterium is often used for contrast matching or contrast variation [48,54–56]. This refers to matching the interaction strength, or scattering length density (SLD), between different parts of the compound to the solvent in which it is dissolved, such that the other parts of the compound become more visible. This SLD variation is achieved by varying the ratio of H:D in the solvent, sometimes in combination with selective deuteration, i.e., exchanging hydrogen for deuterium, in parts of the compound. Tomography studies can exploit this difference in contrast between hydrogen and deuterium, e.g., as a means to track water propagation through porous media or plant roots [57,58]. Due to the strong interaction between hydrogen and neutrons, water flow through dry materials is well captured with NT also without any exchange for deuterium [59–62].

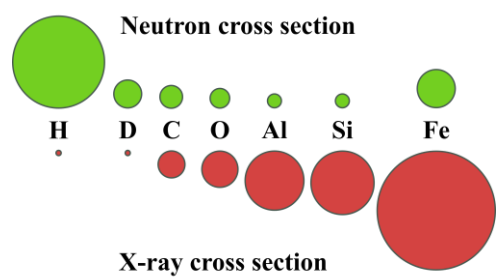


Figure 3.2. Relative interaction strength, indicated by the diameter of the circles, for neutrons and x-rays for a selection of elements.

## Neutron and x-ray sources

Neutrons are generated either by nuclear fission or by spallation [47]. In a research reactor, thermal neutrons are allowed to hit a heavy element nucleus, typically $^{235}$U, causing a fission event. At a spallation source, protons are accelerated towards a heavy metal target, e.g., lead, causing neutrons to be emitted when the protons hit the target nuclei. Most spallation sources are pulsed, which enables time-of-flight (TOF) measurements with a long flight path allowing for

separation of wavelengths. This means that, e.g., monochromatic measurements can be made without the use of monochromators. Both methods of generating neutrons require large-scale facilities. In contrast, x-ray sources for research purposes exist both as large-scale facilities, i.e., synchrotrons and linear accelerators (LINACs), and as lab sources. In the latter, the x-rays are generated by accelerating electrons towards a metal target that emits photons when the electrons interact with the heavy-element metal. At synchrotrons, which are the most common large-scale x-ray facility type, x-rays are generated by accelerating electrons that are then circulated in a storage ring. Bending magnets, wigglers or undulators are used to change their direction, whereupon energy is released in the form of photons, in accordance with Maxwell's equations [63]. A selection of neutron and x-ray large-scale facilities is found in Table 3.1.

Apart from the obvious differences in generating neutrons and x-rays, a main difference between the two probes is the time it takes to do measurements. This discrepancy stems from large differences in flux. The flux of a source represents the integrated intensity of the beam. It is defined as the number of neutrons or x-rays within a 0.1% wavelength range, $\Delta\lambda$, centred around a specific wavelength, $\lambda$, emitted per unit time [64]. Further to this, flux density is often used to account for the size of the irradiated surface and has units [particles/sec/cm$^2$]. Additionally, divergence of the beam is measured by brilliance and has units [particles/sec/cm$^2$/mrad$^2$]. Whilst neutron sources are generally compared by their flux or flux density, x-ray sources are typically described in terms of their brilliance. Collimation is used to reduce beam divergence, at the cost of loss in flux. As can be seen in Table 3.1, neutron sources generally have fluxes that are orders of magnitude lower than x-ray sources. This large difference in flux translates to experimental times being orders of magnitude longer for neutron techniques compared to their x-ray equivalents. Furthermore, for both neutron and x-ray sources, the emitted radiation is polychromatic. Due to the higher flux of a synchrotron x-ray beam compared to that of a neutron source, selecting a narrow bandwidth for the wavelengths, i.e., creating a monochromatic beam, is less critical in terms of lost flux. Having a narrow wavelength distribution is desirable in terms of resolving differences between materials, as contrast is reduced with a wider energy distribution compared to a narrower one. Ultimately, to reach the same spatial resolution with neutrons as with x-rays, significantly longer measurement times are necessary. To improve the usability of neutrons, the European Spallation Source (ESS) is currently (at the time of the writing of this thesis) being built outside of Lund, Sweden. It is expected to yield a flux one order of magnitude higher than any other neutron source in the world (Table 3.1), which will open up new possibilities for studies using neutron techniques.

Table 3.1. A selection of neutron and x-ray sources with location, type of source and particle (n – neutron, ph – photon) output (flux [*/sec], flux density [*/sec/area], brilliance [*/sec/area/mrad$^2$]) specified. For ESS, the output flux is tentative as the source is still in its construction stage. References are given in the table for each specific facility.

| | Facility | Country | Type | Output |
|---|---|---|---|---|
| Neutron sources | ESS [65] | Sweden | Spallation | $1\times10^{18}$ n/sec/cm$^2$ (expected) |
| | SNS [66] | USA | Spallation | $1\times10^{17}$ n/sec |
| | J-PARC [66] | Japan | Spallation | $1\times10^{17}$ n/sec |
| | CSNS [66] | China | Spallation | $1\times10^{16}$ n/sec |
| | ISIS [67] | UK | Spallation | $4.5\times10^{15}$ n/sec/cm$^2$ (peak) |
| | HFIR [68] | USA | Reactor | $2.6\times10^{15}$ n/sec/cm$^2$ |
| | ILL [67] | France | Reactor | $1.5\times10^{15}$ n/sec/cm$^2$ |
| | FRM II [67] | Germany | Reactor | $8\times10^{14}$ n/sec/cm$^2$ |
| | SINQ [66] | Switzerland | Spallation | $4.1\times10^{14}$ n/sec/cm$^2$ |
| X-ray sources | MAX IV [69] | Sweden | Synchrotron | $2.2\times10^{21}$ ph/sec/mm$^2$/mrad$^2$ |
| | PETRA III [69] | Germany | Synchrotron | $2\times10^{21}$ ph/sec/mm$^2$/mrad$^2$ |
| | SPring-8 [69] | Japan | Synchrotron | $2\times10^{21}$ ph/sec/mm$^2$/mrad$^2$ |
| | ESRF [69] | France | Synchrotron | $8\times10^{20}$ ph/sec/mm$^2$/mrad$^2$ |
| | Diamond [69] | UK | Synchrotron | $3\times10^{20}$ ph/sec/mm$^2$/mrad$^2$ |
| | SLS [69] | Switzerland | Synchrotron | $4\times10^{19}$ ph/sec/mm$^2$/mrad$^2$ |
| | Elettra [69] | Italy | Synchrotron | $1\times10^{19}$ ph/sec/mm$^2$/mrad$^2$ |
| | BESSY II [69] | Germany | Synchrotron | $5\times10^{18}$ ph/sec/mm$^2$/mrad$^2$ |
| | ALS [69] | USA | Synchrotron | $3\times10^{18}$ ph/sec/mm$^2$/mrad$^2$ |

# Small-angle scattering

## *Theory*

One mode of interaction between neutrons or x-rays and materials is through scattering. Repetitive structures inside a specimen will cause the incident beam to scatter. The scattering can be either elastic or inelastic. The former causes a change in direction between the incident and scattered particle, and the latter causes a change in both direction and energy [70]. The change in energy is related to the dynamics of the material, whilst the change in direction is related to momentum transfer, $q$, and gives information about the material structure. Furthermore, a scattering event can be either coherent, i.e., give rise to constructive interference, or incoherent. The cross section, i.e., scattering probability, for these events differ with elements and, for neutrons, isotopes. Hence, the total scattering cross section ($\sigma_{sc}$) for a material is the sum of the coherent and incoherent cross sections, $\sigma_{sc} = \sigma_{coh} + \sigma_{incoh}$. Only the coherent component of the scattered radiation contains structural information, as it reports on the relative positions of the scattering particles. Conversely, the incoherent scattering gives the position of only one particle in relation to all others. The incoherent scattering is isotropic and results in a static background signal in the collected scattering data.

SAS arises from colloidal structures, typically 0.5-500 nm in size, and yields structural information in terms of size distribution and orientational alignment [51]. Analysis of the scattering data is, by convention, done in reciprocal space by defining the scattering vector, $q = |\vec{q}|$, as the difference between the wave vectors of the incident ($\vec{k}_i$) and scattered ($\vec{k}_s$) beams (Figure 3.3a). For elastic scattering, i.e., $|\vec{k}_s| = |\vec{k}_i| = \frac{2\pi}{\lambda}$, where $\lambda$ is the wavelength of the incident beam, the relationship between $q$, the angle $\varphi$ between the incident and scattered beam, and the size $d$ of the scattering structure is

$$q = \frac{4\pi}{\lambda}\sin\left(\frac{\varphi}{2}\right) = \frac{2\pi}{d} \qquad 3.1$$

The probed length scale range is determined by the incident wavelength, $\lambda$, as per Equation 3.1, and the sample-to-detector distance (SDD) (Figure 3.3b). Typically, a wavelength of ~1 Å is used in SAXS experiments whilst SANS uses ~4-6 Å [54]. Hence, SANS is acquired at slightly larger angles than SAXS. As $q$ is wavelength dependent, a polychromatic beam results in a distribution of $q$, i.e., smearing of the features in the scattering pattern. The 2D scattering data can, e.g., be analysed as a function of the $q$ vector, $I(q)$, yielding structural information such as particle size and distribution, and as a function of azimuthal angle, $I(\theta)$, yielding information about the alignment of the scattering structures. Reduction of the 2D data to 1D is done by binning all detector pixels with the same radial distance, $q$, to the beam centre for $I(q)$, or with the same azimuthal angle, $\theta$, for $I(\theta)$. The $I(q)$ data yield different structural information in different domains. At

high $q$ (i.e., small length scales), denoted the Porod region, there is contrast only at the interface between the scattering structures and hence the obtainable information relates to the structures' surfaces. In the intermediary region, denoted the Guinier region, the length scales probed relate to the elementary units in the system. From this domain, the so-called form factor, $P(q)$, yields information about the size, shape, and internal structure of one elementary unit. At low $q$, larger length scales are investigated, and information about the structures and interactions of the full system can be obtained through the so-called structure factor, $S(q)$.

The contrast between structures comes from differences in scattering length ($b$) which relates to cross section, as per $\sigma = 4\pi b^2$. For SANS, $b$ differs between elements and isotopes, whilst it for SAXS is directly related to electron density. Hence, the techniques are often complementary and can provide different information. As mentioned earlier, SANS allows for using contrast variation and matching to identify different components of a compound by masking out others. This is done by matching the SLD, $\rho$, of the solvent to that of different parts of the compound by varying the H:D ratio. SLD takes the volume of the scattering particles into account as per $\rho = \sum_i^n b_i/\bar{V}$, where $b_i$ is the scattering length of atom $i$, and $\bar{V}$ is the volume containing the $n$ scattering atoms. Contrast variation works because the coherent scattering length for deuterium is large and positive whilst for hydrogen it is small and negative. Additionally, the incoherent contribution from hydrogen is large whilst it is negligible for deuterium.

## *SAS for bone research*

The first study exploring SAXS as a technique for examining bone was published by Engström and Finean in 1953 [71]. Since then, SAXS has been used extensively to obtain information about the nanostructure of bone. Owing to the recent development towards small beam spot sizes (3-4 $\mu m^2$) and short measurement times (~100 ms), large areas of a specimen can today be mapped by means of scanning SAXS [72].

The main scattering structure is that of the HAp mineral, with only a small contribution coming from the collagen. This collagen signal is often overshadowed by the much stronger signal from the mineral phase. Albeit weak, the collagen signal can be seen as concentric rings as the periodicity of the axially staggered arrangement of the collagen molecules give rise to diffraction peaks. The position of these peaks yields information about the intramolecular D-spacing (~670 Å). In the $q$-range typically probed for bone tissue measurements ($5\times10^{-3}$-$5\times10^{-1}$ $Å^{-1}$), the only observable dimension of the mineral plates is the thickness. The mineral plates are mainly oriented parallel with the collagen fibres and the degree of polydispersity of plate thickness is large [11,31,73]. Hence, the mineral gives rise to a diffuse anisotropic scattering pattern with dominating scattering perpendicular to the fibre orientation (Figure 3.3c). From this scattering, the thickness and organisation of the mineral plates can be acquired.

Thickness can be obtained by fitting of the radially integrated $I(q)$ data [7,38] (Figure 3.3c, d), whilst alignment can be obtained from the azimuthally integrated $I(\theta)$ data [38,74] (Figure 3.3c, e).

The structural information obtainable by SAXS has been utilised, e.g., to better understand the mineralisation process during maturation and growth, differences between healthy and diseased bone, changes during healing, and alterations due to aging. It has been found that maturation and growth result in an increase in thickness and in the mineral becoming more aligned with the main axis of the bone [7,37]. In healthy mature bone, the mineral plates have been observed to be ~30 Å thick and aligned with the collagen fibres [31,37–39,75]. Conversely, the mineral plates in newly formed bone after a fracture are thinner and have a lower degree of orientation [74]. Similar observations have been made when looking at the interface between bone and metallic implants, i.e., newly formed peri-implant bone presents with thinner mineral plates than older bone [72,76]. Moreover, SAXS has been used to study the effects of some drug treatments [38,77] and disease such as osteoporosis, where a thickening of the mineral plates has been observed [37,78]. Furthermore, SAXS has been combined with other techniques such as Fourier transform infra-red spectroscopy (FTIR), Raman spectroscopy, or x-ray fluorescence (XRF). The results yield complementing information about type, amount, and organisation of the chemical constituents in both the mineral and the organic collagen matrix [5,39]. The contribution from the collagen structure on the SAXS signal has also been examined, e.g., in terms of changes during aging. There it was found that increased cross-linking with age causes stiffening of the collagen fibrils and result in a stronger scattering due to increased order [75].

The neutron equivalent to SAXS, i.e., SANS, has had only limited usage in bone research. Apart from the second study presented in this thesis, the author is only aware of two other studies employing SANS for bone structure characterisation [79,80]. However, neutron diffraction (ND) has been used to study, e.g., the mineral plates in terms of size [12–14], and orientation close to implants [15–17], as well as to examine the collagen matrix in terms of molecular spacing in bone [18–20], and in mineralised and non-mineralized tendon tissue [21,22]. In these studies, neutrons were chosen over x-rays mainly due to their penetrating power that allow for larger specimens to be used, but also because of the reduced influence of the mineral on the collected data. Aside from the difference in probed length scales compared to SANS, these ND studies indicate that SANS could have potential as a technique for structural characterisation in bone research.

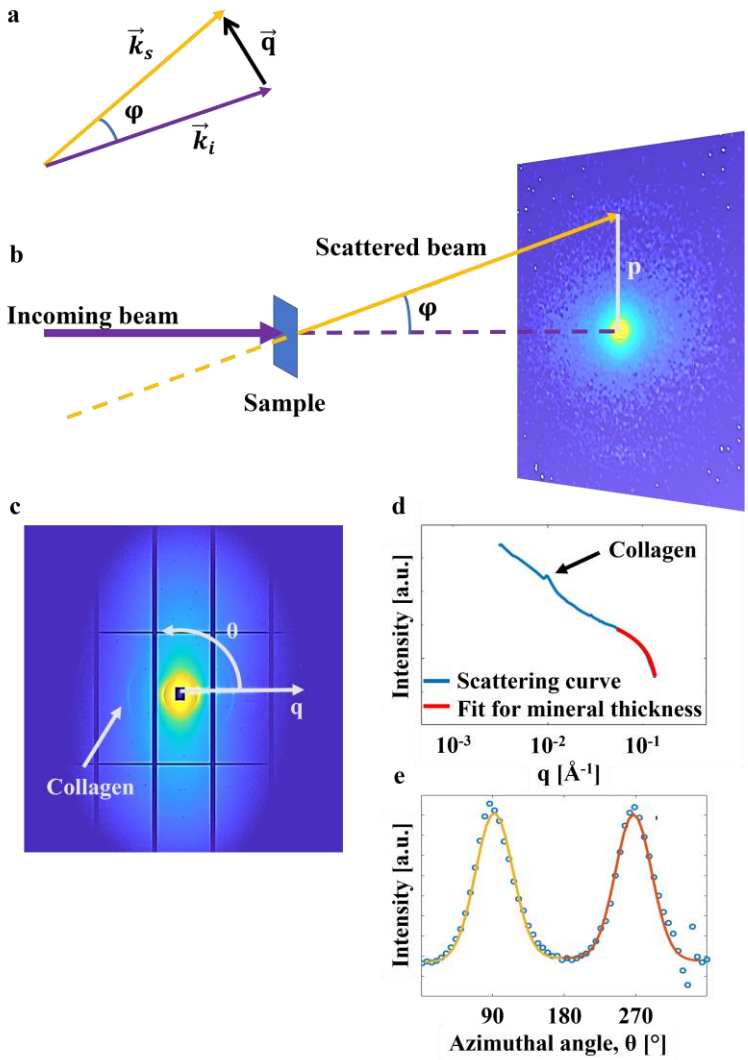


Figure 3.3. Principle of SAS. a) An incoming beam (purple), with wave vector $\vec{k}_i$, interferes with repeating structures in a material. The scattered beam (orange), with wave vector $\vec{k}_s$, scatters to an angle of $\varphi$. The difference between the incident and scattered beams defines the scattering vector $\vec{q} = \vec{k}_s - \vec{k}_i$. b) Schematic presentation of a scattering experiment setup, showing the 2D scattering map registered by the detector bank. Repeating structures in the sample scatter to a position on the detector at the distance p from the centre of the incident beam. c) Characteristic SAXS pattern from cortical bone with a diffuse component from the mineral and sharp rings from the collagen. d) $I(q)$ curve obtained by radial integration of the scattering pattern in (c). e) $I(\theta)$ curve obtained by azimuthal integration of the scattering pattern in (c).

# Tomographic imaging

## *Theory*

Computed tomography is a non-destructive 3D imaging technique used to visualise internal structures in an object. By acquiring multiple 2D images from multiple angles around an object, a 3D image volume of the object can be computed using reconstruction algorithms [81]. Most commonly, the information gathered is the attenuation of the incident radiation. As the interaction probability for neutrons or x-rays differs between elements and the amount of material, different intensities in the images relate to different material composition and density. The attenuation of monochromatic neutrons and x-rays as they pass through a material is caused by a combination of absorption and scattering. This can generally be described by the Beer-Lambert law [50,82] (Equation 3.2).

$$I = I_0 e^{-\sum \mu_i d_i} \tag{3.2}$$

Here $I$ is the intensity of the transmitted beam, $I_0$ is the intensity of the incident beam, $\mu_i$ is the linear attenuation coefficient for material $i$, and $d_i$ is the path length in the material $i$. As $\mu$ is wavelength dependent, the attenuation of a polychromatic beam needs a generalisation of Equation 3.2 into Equation 3.3.

$$I = \int_{\lambda_{min}}^{\lambda_{max}} I_0(\lambda) e^{-\sum_{i=1}^{n} \mu_i(\lambda) d_i} d\lambda \tag{3.3}$$

The interaction between neutrons and matter is weaker than that of x-rays. This means that neutrons have greater penetration power than x-rays, and thicker objects can be imaged with NT than with XRT. However, the lower interaction also means that measurement times are longer.

The spatial resolution obtainable for NT is lower than for XRT in part due to lower brilliance of the neutron beam. Whilst XRT can reach sub-micrometre resolution [83], NT is thus far limited to the micrometre range [84,85]. Depending on the type of radiation source, magnification is achieved in different ways. For a lab x-ray source, radiation is emitted in a cone that projects a magnified image onto the detector [86]. This geometrical magnification, $M$, can be expressed as $M = L/(L - l)$, where $L$ is the distance between the collimator and the imaged object, an $l$ is the distance between the object and the detector [87]. Optical magnification using lenses are necessary for parallel beam geometries, i.e., beams generated at large-scale neutron facilities and synchrotrons. However, perfectly parallel beams are difficult to produce. Hence, there is beam divergence also at large-scale facilities, especially for neutrons. This beam divergence can cause blurriness in the images. The image blur, $d$, can be expressed in terms of $L$ and $l$, as $d = l/(L/D)$, where $D$ is the collimator diaphragm dimension and $L/D$ is the collimation ratio [47,82]. From this, it is clear that the imaged object should be placed as close to the detector as possible to optimise image sharpness. Also, as $L$ is most often fixed, reduced image blur can be obtained by reducing the

collimator diaphragm dimension, $D$, leading to a larger collimation ratio, i.e., a more parallel beam. However, such a reduction in beam size equates to a reduction in flux and, hence, longer exposure times are necessary for adequate signal-to-noise ratio (SNR). The high brilliance of synchrotron x-ray beams means than neither $l$ nor the reduction in flux with increased collimation has a large effect on imaging times. For neutrons, however, the reduction in flux results in increased measurement times.

### *Image artefacts*

Image artefacts degrade image quality and make analysis more challenging. There are numerous types of artefacts [53,88,89]. One of the potentially most detrimental image artefacts in bone research are metal artefacts that occur in the vicinity of metallic implants when using XRT as the imaging modality. When imaged with x-rays, metallic objects can give rise to different types of artefacts, common ones being scattering, beam hardening, and streaking (Figure 3.4).

As the attenuation of the incident beam is wavelength dependent (Equation 3.3), only higher energy x-rays in a polychromatic beam will pass through the full depth of an object consisting of high atomic number materials such as a metallic implant, whereas lower energy x-rays pass through thinner regions of the material. This results in a cupping effect, where the central parts of the object appear darker in the reconstructed images (i.e., lower reconstructed attenuation coefficient) than more peripheral parts, despite consisting of the same material (Figure 3.4a). This effect is known as beam hardening. By filtering out lower energies from the beam, the effect is reduced as fewer (low energy) x-rays are completely attenuated by the material. However, for low-attenuation materials, high-energy x-rays are unwanted as they reduce the contrast in the images by simply passing straight through the imaged object. Hence, if the difference in attenuation between different materials is large, the choice of energy range can become challenging. This is the case for metallic implants imaged with x-rays. For the energy ranges typically used in bone research (12-140 keV) the most prominent interactions between x-rays and tissue-like materials are photoelectric absorption and Compton scattering [50]. The latter causes a change in direction of the incident x-ray photon, so that the scattered photon does not hit the detector at a position straight behind its origin. Hence, it will yield an erroneous contribution to the detected signal in the detector pixel it hits whilst simultaneously detracting from the signal in the target pixel. This can result in shadows, streaks, or glow in reconstructed images (Figure 3.4b). For metals with high linear attenuation coefficient in the energy ranges used to image bone few photons penetrate through the implant, resulting in a low or non-existent detector signal. Due to how the tomographic images are reconstructed from the projections, the noise in the regions with low photon signal is enhanced, resulting in streaking artefacts, i.e., bright and dark bands close to the implant (Figure 3.4c). Whilst beam hardening is more significant for XRT, it can also occur with NT.

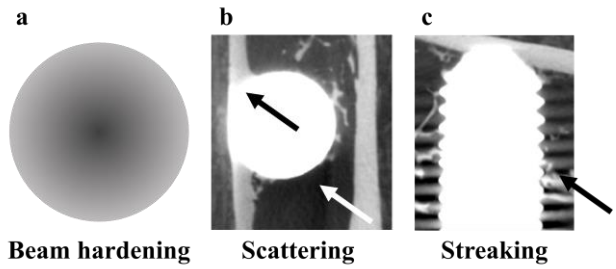


Figure 3.4. Metal image artefacts. a) Sketch of cupping effect caused by beam hardening. b) Scattering and c) streaking caused by a steel implant (images borrowed with permission from [23]).

## *Tomographic imaging in bone research*

XRT imaging was developed in the early 1970s and has since had an immense impact in bone research [90,91]. Due to the contrast between bone and soft tissue, XRT is state-of-the-art for visualising the structure of bone in 3D and has applications ranging from clinical diagnostics of whole bones on the macroscale to high resolution nanotomography in basic research [83,91,92]. As the number of applications are vast, only a small selection related to the topic of this thesis will be mentioned here.

XRT offers a combination of contrast and high resolution that enables characterisation of, e.g., bone volume density, porosity, microstructural organisation, and trabecular architecture [53,93–97]. Such parameters are of interest when developing bone filling substitutes and scaffolds for bone regeneration [98], when evaluating the effects of different treatments on bone formation [99,100], and for characterising bone-implant integration [86,101,102]. Furthermore, because of the linear relationship between x-ray attenuation coefficient and atomic number, tissue mineral density (TMD) can be obtained by comparing the grey values (attenuation coefficient values) to those in images of phantoms with known mineral density [103]. Lab source XRT can provide images with micrometre resolution at relatively short imaging times [91]. Due to the high brilliance, synchrotron sources provide higher resolution (~1/10 μm), lower SNR, and shorter imaging times than lab sources [86,95]. The short imaging times make it more practical to study evolving phenomena such as deformation due to mechanical loading. For example, by acquiring multiple tomographies at different stages of in-situ loading, digital volume correlation (DVC) can be used to calculate internal strains to, e.g., help understand failure mechanisms [104,105].

Applications of NT in bone research are so far highly limited. To the best of the author's knowledge, apart from emerging applications in palaeontology, the only studies (currently 4) employing NT in bone research come from the research group the author belongs to, one being the third study presented in this thesis. In these studies, we compared structural parameters obtained from NT and XRT images of the same specimen [23], explored the potential of using NT to

investigate bone-implant integration mechanically using DVC [24], and compared NT to XRT [26] and to histology [25]. The results showed that NT offers advantages compared to XRT when studying the structure and mechanical properties of bone in the close vicinity of metal implants where image artefacts in the XRT data can make it difficult to, e.g., track crack movement during loading of the implant [101]. In addition, comparison to histology has highlighted the potential of NT for looking at soft skeletal tissues [25].

Since the attenuation of a material can vary for NT and XRT, so can the contrast between different materials. This makes the two modalities highly complementary. In archaeology, NT is used increasingly to differentiate between material phases with similar x-ray attenuation coefficients. Both metallic artefacts and fossilised biological specimens [106–114] have been imaged with NT and the resulting images show contrast between material phases that would not be present had XRT been utilised. The complementary nature of NT and XRT has also been exploited in research fields such as geology, geomechanics and for studying porous media [57,60,115–117]. In these studies, dual modality data has yielded an increase in information about the imaged object. Furthermore, a recent study employed NT as part of a multimodal approach to study corrosion in biodegradable implants [118]. These studies, together with the aforementioned NT studies performed by our research group, implies a significant potential for the use of NT in bone research.

## 3.3 Mechanical testing

The mechanical properties of a material at different length scales can be characterised by means of mechanical testing. By applying a load or a displacement to the material, and registering the resulting force and displacement data, extrinsic mechanical properties can be derived. A stress-strain curve can be calculated by taking the shape of the specimen into account, from which intrinsic mechanical properties can be obtained [119,120]. For bone tissue, the most relevant intrinsic mechanical parameters are:

- yield and ultimate stress and strain (i.e., stress and strain at the limit between elastic and plastic behaviour and at failure)
- Young's modulus (i.e., the slope of the linear region)
- toughness (i.e., the area under the stress-strain curve until failure).

Mechanical testing can be performed at different length scales depending on the research question. The different tissue types (cortical and trabecular) exhibit different mechanical behaviours. On the organ scale, the combination of the tissue types, together with the specific shape of the bone, all contribute to the global mechanical properties. For characterising the mechanical properties of the individual bone tissues, each specific tissue type needs to be isolated.

In this thesis, compression testing of trabecular bone plugs was carried out as part of study IV. Hence, the focus here will be on the mechanical characteristics of trabecular bone. For a more complete description of bone mechanical properties, the reader is referred to, e.g., [121–126].

Mechanical characterisation of trabecular bone is commonly done by compression testing. These tests are realised by applying a compressive force or displacement to a specimen whilst simultaneously recording changes in both parameters. By using small (5-50 mm) cylindrical or cubic specimens, structural homogeneity of the sample can be assumed, and intrinsic material properties can be derived. As trabecular ultrastructure is optimised for the loading conditions occurring in the specific anatomical site, the mechanical properties vary depending on anatomical origin [127,128]. Studies have found that also strain rate, specimen shape, and specimen dimensions influence the measured mechanical behaviour [129,130]. Furthermore, the bone marrow found in the trabecular bone porosities has an effect on the compression behaviour with lower elastic modulus (26%) and maximum stress (38%) compared to when the marrow is removed [131]. Bone volume fraction (apparent BV/TV) has been shown to be the morphological parameter that most affects stiffness in trabecular bone [132,133]. Hence, when examining the mechanical parameters of a set of specimens, differences in BV/TV should be accounted for. BV/TV varies between species and anatomical locations [127,134–136]. Thus, by harvesting specimens from different locations in a skeletal bone obtained from one individual, variation in mechanical properties due to BV/TV can be accounted for whilst simultaneously reducing possible inter-individual influence. The mechanical properties of bone are also dependent on the hydration state of the tissue. Studies have shown that bone tissue exhibits increased stiffness with increased dehydration at multiple hierarchical levels [137–140]. Hence, it is important to monitor hydration levels during testing to account for possible deviations in the obtained mechanical properties. Few studies have investigated how rehydration affects the mechanical behaviour. However, studies on the flexural properties of cortical bovine bone and whole mouse femora concluded that rehydration reverts the changes caused by drying [139,141]. In both studies, the specimens were dried in air for a prolonged amount of time (25 days for the cortical bone and 48 h for the mouse femora) before being rehydrated. Both studies found that 3 h was sufficient for the mechanical properties to revert to such an extent that no statistically significant differences were seen compared to the non-dried-and-rehydrated bone.

# 4. Material & Methods

In this chapter, the material and methods used in this thesis are outlined. First, the samples used in each individual study are described. The methods for the SAS experiments in study I and II are then detailed, followed by the methods used for tomographic imaging in each of the four studies, and the mechanical testing carried out in study IV. Finally, a description of the methods used for analysis of the acquired data is presented.

## 4.1 Samples

### Cortical bone from rabbits (Study I)

Specimens consisted of cortical bone from the mid-diaphysis of the left humeri of female New Zealand White rabbits, harvested from five age groups (sacrificed at newborn (NB), 11 days, 1 month, 3 months, and 6 months of age). The sample collection was approved by the Animal Care and Use Committee of the University of Eastern Finland. Perpendicular sections (longitudinal and radial) with an average thickness of 140 μm were cut in the mid-diaphyseal region. Each age group was represented with n = 4-6 sections in both longitudinal and radial orientation except for the 3-months-old specimens, from which only longitudinal sections were obtained.

### Cortical bone from cow, sheep, and pig (Study II)

Specimens consisted of cortical bone from one bovine (29 months old) and one porcine (6 months old) femora, as well as one ovine (7 months old) tibia, all obtained from the local abattoir. Perpendicular sections (longitudinal and radial) with an average thickness of 1 mm were cut in the mid-diaphyseal region.

## Rat tibiae with metal implants (Study III)

Specimens consisted of proximal rat tibiae with a hollow titanium screw (Ø = 3.5 mm, h = 6.3 mm) implanted in the proximal diaphysis. All screws were filled with a biomaterial (calcium sulphate/hydroxyapatite). Male Sprague Dawley rats (~10 weeks old), procured from Taconic (Denmark) were divided into two groups, a control group (Ctrl, n = 5), and a treated group (Trtd, n = 6) where the biomaterial was mixed with bioactive molecules (zoledronic acid and recombinant human bone morphogenic protein-2). The protocol followed a previous study where the effects of these drugs on increased peri-implant bone formation were investigated in more detail [99]. The implant was placed transversely to the longitudinal axis of the bone and left to integrate for six weeks before the rats were euthanised by $CO_2$ asphyxiation, as detailed in Raina et al. (2019) [99]. The tibiae were dissected, cleaned from soft tissue, and sectioned approximately 25 mm from the proximal epiphysis, before being immersed in physiological saline solution and frozen. The animal study was carried out in accordance with ethics guidelines and approved by the Swedish Board of Agriculture (permit numbers: M79-15 and 15288/2019).

## Rat tibiae and trabecular bovine bone plugs (Study IV)

Specimens consisted of proximal tibiae from male Sprague Dawley rats and trabecular bovine bone plugs. The Sprague Dawley rats (~10 weeks old) were procured from Taconic (Denmark). The rats were euthanised by $CO_2$ asphyxiation. The tibiae (N = 3) were dissected, cleaned from soft tissue, and sectioned approximately 25 mm from the distal epiphysis. The use of the animals was approved by the Swedish Board of Agriculture (permit numbers: M79-15 and 15288/2019). Trabecular bovine bone plugs (N = 75, Ø = 6 mm, h = 10 mm) were extracted from different anatomical locations (major trochanter, head, neck, and metaphysis) in the proximal femurs of adult (28-29 months) heifers, procured from the local abattoir.

To explore how the amount of $D_2O$ in bone specimens affects NT images, the rat tibiae were dried in vacuum (-25 inHg) at ambient temperature for 16 h before being imaged with NT (Figure 4.1a). They were then rehydrated by immersion in salinated $D_2O$ (0.9% NaCl) for ~12 h and imaged again. Two of the three specimens were rehydrated further and imaged again after ~30 h and ~35 h, respectively. To elucidate how drying and rehydrating bone specimens affect bone mechanical properties, the trabecular bone plugs were divided into three groups such that three hydration states could be compared: control, dried, and rehydrated (Figure 4.1b). Mechanical testing was carried out during three experimental campaigns and the hydration protocols varied slightly, as detailed below. All specimens were weighed before and after each step of the hydration protocol to assess weight loss and gain due to drying and rehydration.

Experimental campaign I - specimens imaged with NT (N = 18)

- Control (n = 6) – soaked in salinated $D_2O$ (0.9% NaCl) for 48 h to exchange the inherent $H_2O$ for $D_2O$ by diffusion
- Dry (n = 6) – dried in vacuum (-25 inHg) at ambient temperature for 3 h
- Rehydrated (n = 6) – dried in vacuum (-25 inHg) at ambient temperature for 3 h before being immersed in salinated $D_2O$ (0.9% NaCl) for 48 h

Experimental campaign II (N = 30)

- Control (n = 10) – frozen immediately after harvest
- Dry (n = 10) – dried in vacuum (-25 inHg) at ambient temperature for 3 h
- Rehydrated long (n = 10) – dried in vacuum (-25 inHg) at ambient temperature for 3 h before immersion in physiological saline solution (0.9% NaCl, $H_2O$) for 48 h

Experimental campaign III (N = 27)

- Control (n = 9) – frozen immediately after harvest
- Dry (n = 9) – dried in vacuum (-25 inHg) at ambient temperature for 3 h
- Rehydrated short (n = 9) – dried in vacuum (-25 inHg) at ambient temperature for 3 h before immersion in physiological saline solution (0.9% NaCl, $H_2O$) for 3 h

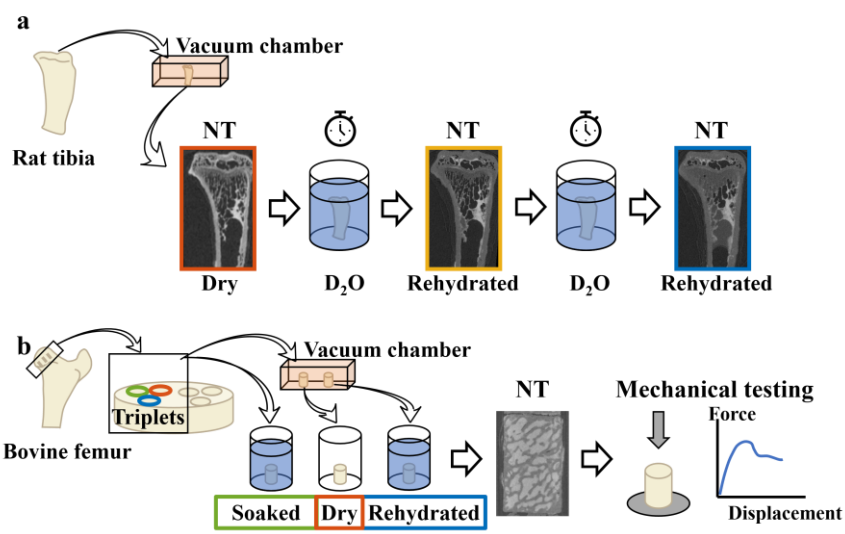


Figure 4.1. Overview of the experimental procedure in study IV. a) Proximal rat tibiae (N = 3) were dried in vacuum before being imaged with NT. The tibiae were then rehydrated in $D_2O$ and imaged again. Two of the specimens were further hydrated and imaged a third time. b) Trabecular bone plugs (N = 75) were extracted from bovine femora. Triplets (plugs extracted next to each other) were divided into three groups that were subjected to three different hydration protocols. A subset (n = 18, 6 plugs per hydration state) plugs were imaged with NT. All plugs were tested mechanically to assess possible changes in mechanical properties caused by the drying and rehydration.

## 4.2 Small-angle scattering (Studies I-II)

### SAXS for studying mineralisation in cortical bone (Study I)

2D scanning micro-focused SAXS measurements were carried out during two beamtimes at the cSAXS beamline, Swiss Light Source, Paul Scherrer Institut (PSI), Villigen, Switzerland [142]. During the first beamtime, radial samples were measured mounted on Kapton tape, using a beam energy of 12.4 keV, equivalent to an x-ray wavelength of 1 Å, with a SDD of 7.1 m, beam size of 5.5×4 μm$^2$, step size of 5 μm (resulting in 5×5 μm$^2$ pixel size in raster-scan), and an exposure time of 30 ms per scan point. During the second beamtime, longitudinal samples were measured using the same parameters as above except that the exposure time was 100 ms and no Kapton tape was used. In both cases, a Pilatus 2 M detector bank [143] with 1475×1679 pixels (172×172 μm$^2$ pixel size), was used to collect scattering data in the $q$-range 0.03-1.75 nm$^{-1}$. For all measurements, a calibrated microscope was used to define regions of interest. Depending on the thickness of the cortex, areas between 0.12 and 0.91 mm$^2$ were scanned using continuous line scans. AgBe was used for calibration of the q-range. Additional measurements on a single piece of Kapton tape were performed to subtract the signal from the measurements of the radial samples.

### SANS and SAXS from cortical bone for nanostructure characterisation (Study II)

SANS measurements were carried out at the D11 beamline, at the Institut Laue–Langevin, Grenoble, France [144]. The specimens were placed in 2 mm quartz cuvettes (100-QS, Hellma Analytics) for single point measurements. A wavelength of 5.6 Å in combination with SDDs of 39 m, 8 m, and 1.4 m were utilised to acquire data in the $q$-range 0.00046-0.36 Å$^{-1}$ (Figure 4.2a), using CERCA detectors with pixel size of 3.75×3.75 mm$^2$. The beam spot size was Ø 2 mm. An empty cuvette was measured to account for background.

SAXS measurements were carried out at the cSAXS beamline, Swiss Light Source, Paul Scherrer Institut (PSI), Villigen, Switzerland [142]. The specimens were mounted directly on the specimen stage and were hence measured in air. A beam energy of 12.4 keV, equivalent to an x-ray wavelength of 1 Å, in combination with a SDD of 7.1 m were utilised to acquire data in the $q$-range of 0.0048-0.109 Å$^{-1}$ (Figure 4.2b), using a Pilatus 2 M detector with pixel size 172×172 μm$^2$ [143]. The beam size at the specimen position was 150×125 μm$^2$. A 2D grid scan of 8×9 points was performed to cover an area of 1.2×1.125 mm$^2$ centred at the same positions as measured previously with SANS.

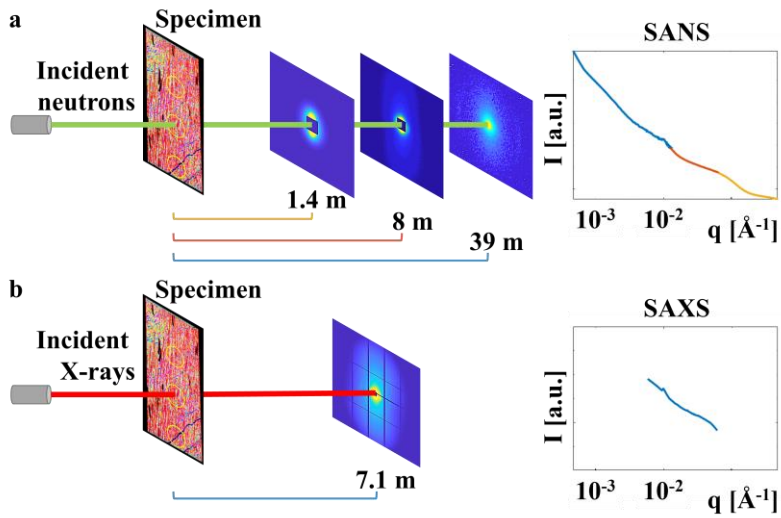


Figure 4.2. Experimental setup for study II. a-b) Experimental setup for SANS and SAXS, respectively, specifying distances between specimen and detector, and the resulting $q$-ranges (log-log scale).

## 4.3 Tomographic imaging (Studies I-IV)

### XRT for tissue mineral density assessment (Study I)

XRT measurements were carried out using a Skyscan 1172 (Skyscan, Aartselaar, Belgium). Energy settings of 100 kV and 100 µA were used, with a 0.5 mm aluminium filter and eight-repeated scans. Due to the large spread in size between younger and older specimens, different isotropic voxel sizes were used (14.8 µm for NB and 11 days, 21.7 µm for 1 month, and 34.6 µm for 3 months and 6 months) to image as much of each specimen as possible. Image reconstruction was performed by correcting for ring artefacts and beam hardening (20%) (SkyScan NRecon package v. 1.5.1.4). A water phantom and two HAp phantoms (0.75 g/cm$^3$ and 0.25 g/cm$^3$, respectively) were imaged with each set of imaging settings. Calibration of TMD was carried out according to the system manufacturer's protocol.

## XRT for structural characterisation of cortical bone (Study II)

XRT measurements were carried out using a ZEISS Versa XRM52 at the 4D Imaging Lab, Division of Solid Mechanics, Lund University, Sweden. A tube voltage of 80 kV and power of 70 W were used to collect 2501 projections over 360°, each with 5 s exposure. The field-of-view (FOV) was 18×18 $mm^2$, and the isotropic voxel size in the reconstructed images was 9.25 µm. Two HAp phantoms (0.75 $g/cm^3$ and 0.25 $g/cm^3$, respectively) were imaged to calibrate the TMD of the specimens.

## NT and XRT of rat tibiae with metal implants (Study III)

Dual modality tomographic imaging was carried out at the NeXT-Grenoble beamline at Institut Laue-Langevin (ILL), Grenoble, France [84]. Each specimen was mounted vertically, with the proximal epiphysis facing upwards, and placed as close to the detector as possible. The dual NT and XRT setup at NeXT-Grenoble enabled imaging with NT followed by XRT without moving the specimen.

For the NT, 1200 projections, covering a FOV of 41×41 $mm^2$, were acquired over 360° rotation using a pinhole of 23 mm (D). The exposure time was 2 seconds per projection and 3 projections per angle were averaged to reduce noise. The resulting virtual isotropic voxel size was 18.6 µm. Due to the large collimation distance (L ≈ 10 m), the neutron beam at the specimen position was considered parallel. By placing the specimen as close as possible to the detector, the measured spatial resolution was close to 46 µm (L/D ≈ 435). For XRT, 1312 projections were acquired over 360° rotation, covering the same FOV as for the NT. The source voltage and current were 110 kV and 160 µA, respectively, in combination with a frame rate of 9 Hz, and averaging 5 projections per angle to reduce noise. The resulting virtual isotropic voxel size was 24.4 µm. Both neutron and x-ray projections were normalised for beam inhomogeneities and background noise in the scintillators and cameras, before being reconstructed using the filtered-back-projection technique as implemented in the commercial software X-Act (RX Solutions, Chanavod, France).

## Effects of hydration state on NT images of bone (Study IV)

NT of rat tibiae and trabecular bovine bone plugs (n = 18) was carried out at the NeXT-Grenoble beamline at ILL, France [84]. XRT of all bone plugs (N = 75) was carried out at the NeXT-Grenoble beamline (n = 18) and at the 4D Imaging Lab, Division of Solid Mechanics, Lund University, Sweden (n = 57).

For NT of the rat tibiae, 1792 projections, covering a FOV of 13.5×13.5 $mm^2$, were acquired over 360° rotation using a pinhole of 30 mm. The exposure time was 3 seconds per projection and 3 projections per angle were averaged to reduce noise. The resulting virtual isotropic voxel size was 7.15 µm. The collimation distance was ~10 m, yielding L/D ≈ 333. For NT of the bovine trabecular bone plugs (n = 18), 992 projections, covering a FOV of 32×32 $mm^2$, were acquired over 360° rotation using a pinhole of 23 mm. The exposure time was 3.5 seconds per projection and 3 projections per angle were averaged to minimise noise. The resulting virtual isotropic voxel size was 15.6 µm. The collimation distance was ~10 m, yielding L/D ≈ 435. Without moving the specimens, XRT was done using a source voltage and current of 110 kV and 160 µA, respectively. 1312 projections were acquired over 360° rotation, covering the same FOV as for the NT. The frame rate was 9 Hz and 5 projections per angle were averaged to reduce noise. The virtual isotropic voxel size was 24 µm. The neutron and x-ray projections for both tibiae and bone plugs were normalised for beam inhomogeneities and background noise in the scintillators and cameras, before being reconstructed using the filtered-back-projection technique as implemented in the commercial software X-Act (RX Solutions, Chanavod, France).

The trabecular bone plugs that were used only for analysing the mechanical properties (n = 57) were imaged with XRT using a ZEISS Versa XRM52. Source voltage and current were 80 kV and 87 µA, respectively. 1001 projections were acquired over 360° rotation, covering a FOV of 14×14 $mm^2$. The exposure time was 1 sec, and the virtual isotropic voxel size was 13.5 µm. Reconstruction was performed using the filtered-back-projection technique as implemented in the ZEISS reconstruction software.

## 4.4 Mechanical testing (Study IV)

### Effects of hydration state on mechanical properties of bone (study IV)

Trabecular bovine bone plugs (N = 75) were tested in unconfined uniaxial compression (Instron® 8511.20, Instron Corp). After applying a pre-load of 15 N, a constant displacement rate of 1 mm/sec was used to compress the specimens. Force and displacement data were collected and converted to stress and strain by normalising for specimen dimensions. Failure was considered as the first clear peak in the resulting stress-strain curves. From the stress-strain curves, intrinsic parameters were calculated, namely peak stress, Young's modulus, and toughness. Considering the specimen specific apparent BV/TV, these parameters were compared between hydration states.

## 4.5 Data analysis

### Small-angle scattering (Studies I-II)

#### *SAXS for studying mineralisation in cortical bone (Study I)*

The 2D scattering data from each scan point were analysed using in-house Matlab code (R2018b, MathWorks Inc., MA, USA) [74]. Using the method described by Turunen et al. (2016) [37], based on Bünger et al. (2010) [38], the average mineral plate thickness was calculated by curve fitting in the 0.32-1.40 $nm^{-1}$ $q$-range. The average mineral plate orientation and degree of orientation were determined as described previously [74]. Thus, for each sample, maps of each parameter were generated. From the maps, scan points without bone tissue were excluded using a specimen specific mask based on the integrated SAXS intensity. The orientation value for each point was corrected by adding/subtracting the tilt of the cortex in the sample setup, such that the long axis was set as 90°.

The structural parameters were investigated as a function of animal age and tissue age. The latter was performed by looking at radial profiles of osteons, from the canal to the interstitial tissue, in the oldest age group where proper osteons had formed. The mineral plate thickness heterogeneity was evaluated from the full width at half maximum (FWHM) of a Gaussian curve fitted to the histogram of the spatial distribution. The goodness-of-fit was checked by means of residuals and a threshold was introduced to exclude bad fits, resulting in the omittance of four samples in the longitudinal group (two from the 1-month group, and one from the 3- and 6-months groups, respectively).

#### *SANS and SAXS for structural characterisation of cortical bone (Study II)*

The 2D SANS data from each scan point were analysed in LAMP [145] and GRASP (GRASansP Barebones v. 8.14, Charles Dewhurst, Institut Laue Langevin, France). Data from each detector configuration were normalised by the intensity of the attenuated direct beam and the corresponding attenuation factor to reach absolute scale intensity. The beamstop and detector edges were masked away, and the data were integrated both over $2\pi$ (full integration), and parallel with and perpendicular to the collagen fibre orientation (partial integration for anisotropy analysis). The partial integration was performed as 10 pixels wide strips around the beam centre and extending well beyond the region where counts were detected. The integrated data from the three configurations were merged using Matlab (R2019a, MathWorks Inc., MA, USA) to have a continuous $q$-range. This was achieved by adjusting the intensities of the mid- and high-$q$ data ranges to overlap the low- and mid-$q$ range data, respectively, using a factor close to 1 (± 10%).

The 2D SAXS data were averaged to simulate the volume measured with SANS. Data reduction, calibration to absolute intensity using a glassy carbon standard [146], and subsequent angular integration were performed using in-house Matlab code (R2019a, MathWorks Inc., MA, USA) [34,37], as well as the cSAXS Matlab base package [147]. The beamstop, edges of the detector modules, and bad pixels were masked away before the data were integrated both over $2\pi$ (full integration), and parallel with and perpendicular to the collagen fibre orientation (partial integration for anisotropy analysis). The partial integration was realised as 30 pixels wide strips around the beam centre and extending well beyond the region where counts were detected.

The integrated scattering intensities from SANS and SAXS were compared in the overlapping $q$-range (0.0048–0.109 $Å^{-1}$). The intensities were adjusted by a proportionality constant, specific to the specimen and measurement position, to overlap at low $q$. The difference between SANS and SAXS intensities at each $q$, defined as the interval between two sequential SANS data points, was calculated to identify $q$-range dependent differences between the techniques. Also, the difference for the entire overlapping $q$-range was investigated. In addition, anisotropy was explored using the partial integration. For this the overlapping $q$-range was slightly smaller due to the reduced SNR at high $q$. Furthermore, integration as a function of azimuthal angle covering four partial $q$-ranges was used to elucidate possible differences in anisotropy as a function of $q$. The anisotropic scattering patterns were further analysed in terms of an order parameter, $S$, quantifying the orientational order of the mineral plates, assuming uniaxial symmetry. Scattering contrast was compared using scattering length densities of collagen and mineral calculated using the NIST Neutron activation and scattering calculator.

# Tomographic imaging (Studies I-IV)

## *Tissue mineral density calculation (Studies I-II)*

Using the imaged HAp phantoms, voxels with a greyscale value corresponding to a TMD above a set threshold (0.20 g/cm$^3$ in Study I and 1.0 g/cm$^3$ in Study II) were considered mineralised tissue. For the specimens in study II, the positions (regions-of-interest, ROI) measured with SANS and SAXS were identified based on known distances obtained from the transmission measurements from the scattering experiments. After segmentation of the mineralised tissue, the average TMD for a specimen (study I) or ROI (study II) was calculated.

## *Microstructural orientation (Study II)*

Using ImageJ v1.52i [148], micro-porosity was visualised by *minimum intensity projection*. Porosity was calculated using BoneJ [149] and microstructural orientation was obtained using OrientationJ [150].

## *Bimodal image registration and joint histogram analysis (Study III)*

The XRT image volumes were registered onto the NT image volumes using the open source SPAM software [151] and the Gaussian mixture model for multi-modal image registration [115,116] (Figure 4.3a). As a by-product, the registration also yields a phase segmentation, where each phase corresponded to a different material phase (Figure 4.3b).

The joint histograms (250×250 bins) were analysed in terms of peak centre position and peak shape to investigate how skeletal tissues and metallic implants are captured with NT and XRT (Figure 4.3a). Peak centre positions were obtained using a custom Matlab script where user input on an initial guess of peak centre positions was used in combination with a peak-finding algorithm (findpeaks.m, Matlab, R2019a, MathWorks Inc., MA, USA). For each peak and specimen-specific joint histogram, a square (70×70 bins) ROI was centred on the identified peak centre position (Figure 4.3c) and a threshold of 75% of the mean intensity inside the ROI was used to remove low intensities. The intensity contributions from each modality (i.e., the "visibility" of the various phases) were evaluated by projecting the peak onto the y-axis (NT) or x-axis (XRT), as defined in Figure 4.3d. FWHM and area-under-curve (AUC) normalised to the total area (TA) covered by the ROI (AUC/TA) (Figure 4.3e), as well as peak centres were compared between modalities, specimens, and treatment groups.

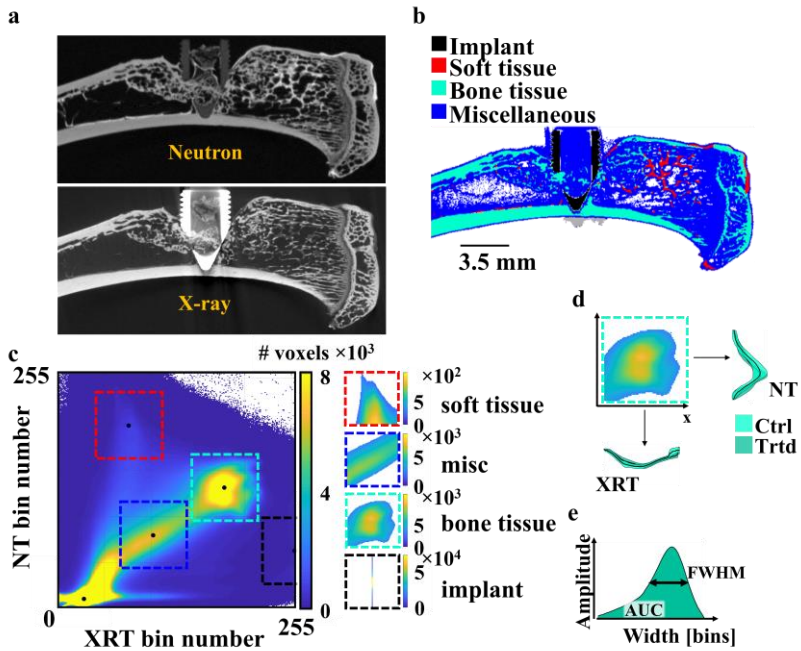


Figure 4.3. Data analysis in study III. Bimodal image registration and joint histogram analysis. a) Midline sagittal slices of registered NT and XRT images for a representative specimen from the Trtd group. b) Phase segmentation of the material phases obtained from the multi-modal image registration of the images in (a). The scale bar refers to both (a) and (b). c) Intensity peaks in the joint histogram, identified as corresponding to soft tissue (red), miscellaneous non-separated structures (misc, blue), high-density bone tissue (mint), and the metallic implant (black). d) The peak corresponding to high-density bone tissue, after thresholding at 75% of the mean intensities inside the ROI. Intensity contribution from treatment groups (Ctrl and Trtd) and modalities (NT and XRT) were obtained by projecting the peak onto each of the histogram axes. The data is shown as the mean of each treatment group and modality (black line) with their respective standard deviation (shaded area). e) Definition of AUC (shaded area under the curve) and FWHM, exemplified using an NT peak from a Trtd specimen.

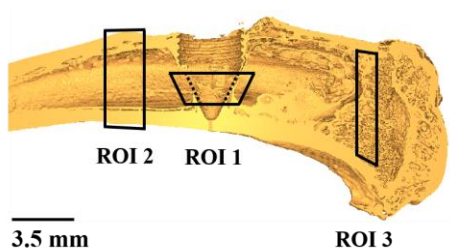


Figure 4.4. Data analysis in study III. Midline sagittal slice through a volume rendering of the segmented bone phase in the NT image of a representative specimen from the Ctrl group. The three ROIs used to quantify peri-implant bone (ROI 1), cortical bone (ROI 2), and soft tissue and trabecular bone (ROI 3) are indicated in black.

### *Volume fraction calculation (Studies III-IV)*

Tissues were segmented using threshold values selected to yield the best visual segmentation for all specimens. Tissue volume fractions were calculated as the ratio between the volume of the segmented tissue and the total volume inside a defined ROI.

In study III, volume fractions were calculated in three different anatomical locations (Figure 4.4). The tissue volume inside each ROI was obtained either from the phase segmentation acquired from the bimodal image registration or from segmentation by means of thresholding in the NT and XRT images. For all ROIs, tissue volume fractions were compared between segmentation approaches. The amount of newly formed bone at the bone-implant interface (ROI 1) was calculated inside a ROI defined using the phase segmentation of the implant. Here, bone volume fraction was compared both between segmentation approaches and treatment groups. The volume fraction of high-density bone tissue inside a ROI distal to the implant (ROI 2) was compared between segmentation approaches for the specimens in the Ctrl group. The volume fractions of soft tissue and trabecular bone inside a ROI in the metaphysis (ROI 3) were between segmentation approaches for the specimens in the Ctrl group.

In study IV, bone volume fraction in the trabecular bone plugs was obtained from the XRT images using the ImageJ plugin BoneJ (v7.09) after segmentation based on thresholding. The edges of the bone plugs were excluded to reduce influence from bone fragments remaining from the extraction process.

### *Image quality assessment (Studies III- IV)*

The contrast between material phases, or between material phases and background was evaluated in terms of contrast-to-noise-ration (CNR), as per Equation 4.1.

$$CNR = \frac{|mean(S_i) - mean(S_{ii})|}{\sqrt{std(S_i)^2 + std(S_{ii})^2}} \quad 4.1$$

Here $mean(S_i)$ is the mean grey value of material phase $i$, and $mean(S_{ii})$ is the mean grey value of material phase $ii$ or of the background. In study III, the material phases high-density bone, soft tissue, and metallic implant were isolated using the phase segmentation obtained from the image registration. In study IV, regions containing background, bone cortex, and $D_2O$ were defined manually in three representative image slices for each dataset.

In study IV, image contrast was further evaluated by looking at line profiles and grey value distributions. In the images of the two tibial specimens rehydrated for > 40 h, line profiles were taken across a region where $D_2O$ was present in the final hydration state, in a representative image slice identified in all hydration states. To look at similar regions, the image volumes were manually aligned using ImageJ (1.53c, National Institute of Health, USA). The line profiles were

assessed in terms of features and intensity. Contrast was also assessed by comparing the grey value distributions in the NT images of the trabecular bovine bone plugs.

## Statistical analysis (Studies I, III, and IV)

In study I, linear mixed-effects analysis was used to test for statistical significance of changes with animal age while considering the high number of measurement points per sample (R Studio, v1.2.1335, RStudio, Inc.). A Kruskal-Wallis test was used to compare spatial heterogeneity of the mineral crystal thickness, the structural parameters from the osteonal profiles, as well as TMD between age groups (Matlab R2018b, MathWorks Inc., MA, USA). Pearson's linear correlation coefficients were used to compare the new SAXS and XRT data with data from polarised light microscopy and spectroscopy from previous studies [5,6]. All statistics were done on a significance level of $p = 0.05$.

In study III, the analysed parameters were not normally distributed, as confirmed by the Shapiro-Wilk normality test. Hence, non-parametric statistical analysis was used to compare peak centre positions, peak shapes (AUC/TA and FWHM), CNR, and volume fractions. Paired parameters obtained from the two modalities (NT and XRT) were compared using the Wilcoxon signed-rank test. Treatment groups (Ctrl and Trtd) were compared using the Mann-Whitney U-test. All statistical analyses were done on a significance level of $p = 0.05$, in Matlab (R2019a, MathWorks Inc., MA, USA).

In study IV, linear mixed-effects analysis was used to assess differences in mechanical properties between hydration groups. The mechanical parameter was defined as the response/dependent variable. BV/TV and hydration state were considered explanatory variables and experimental campaign was used as a random effect to account for possible differences between campaigns. The response variable was log-transformed to correct for heteroskedasticity in the residuals, after which assumptions of homoskedasticity and normality were considered to be met. A quadratic effect of BV/TV was added to correct for a quadratic pattern in the residuals-versus-BV/TV plots. Goodness-of-fit was assessed through root-mean-square-error (RMSE), and adjusted coefficient of determination ($R^2$). All statistical analyses were done on a significance level of $p = 0.05$, in Matlab (R2019a, MathWorks Inc., MA, USA).

# 5. Results

In this chapter, the main results and findings from each study is presented. Each section starts with a short summary of the approach in the study, followed by a summary of the main results.

## 5.1 Mineralisation during maturation and growth (Study I)

SAXS data were acquired from cortical bone specimens cut in perpendicular orientations (radial and longitudinal), obtained from rabbits at different stages of maturation (newborn (NB), 11 weeks, 3 months, and 6 months of age). Mineral plate thickness in both longitudinal and radial specimens, as well as orientation and degree of orientation in the longitudinal specimens were compared between age groups to elucidate changes with animal age. Radial profiles of osteons were analysed to assess changes with tissue age. XRT measurements were performed to obtain TMD. The SAXS data from the radial specimens were compared to mechanical and spectroscopic data collected previously [5,6].

Mineral plate thickness increased with animal age in both longitudinal and radial specimens (Figure 5.1a, b). For the radial specimens, an increase was seen only between the 6-month-old and younger age groups ($p < 0.05$). For the longitudinal specimens, significant changes were seen between all age groups. At 6-months of age, the mineral plate thickness was lower in the radial sections than in the longitudinal. Based on the analysis of the osteonal profiles, a trend of increasing thickness from the inner edge to half of the profile was seen, after which it decreased and seemed to plateau reaching the outer edge (Figure 5.1c). Comparison with spectroscopic data from the same cohort of specimens [5] (Table 5.1) showed correlation with crystal maturation (crystallinity) and bone turnover (carbonate/phosphate and carbonate/amide I). Comparison to mechanical properties indicated a relationship between thickening of the mineral plates and higher elastic stiffness of the tissue. The orientation of the mineral plates in the longitudinal specimens stayed constant at around 90° (i.e., parallel with the long axis of the bone), whilst the degree of orientation increased with animal age (Figure 5.1a). TMD was found to increase with animal age up to 3 months of age. Changes in TMD and mineral plate thickness were highly correlated in the longitudinal specimens.

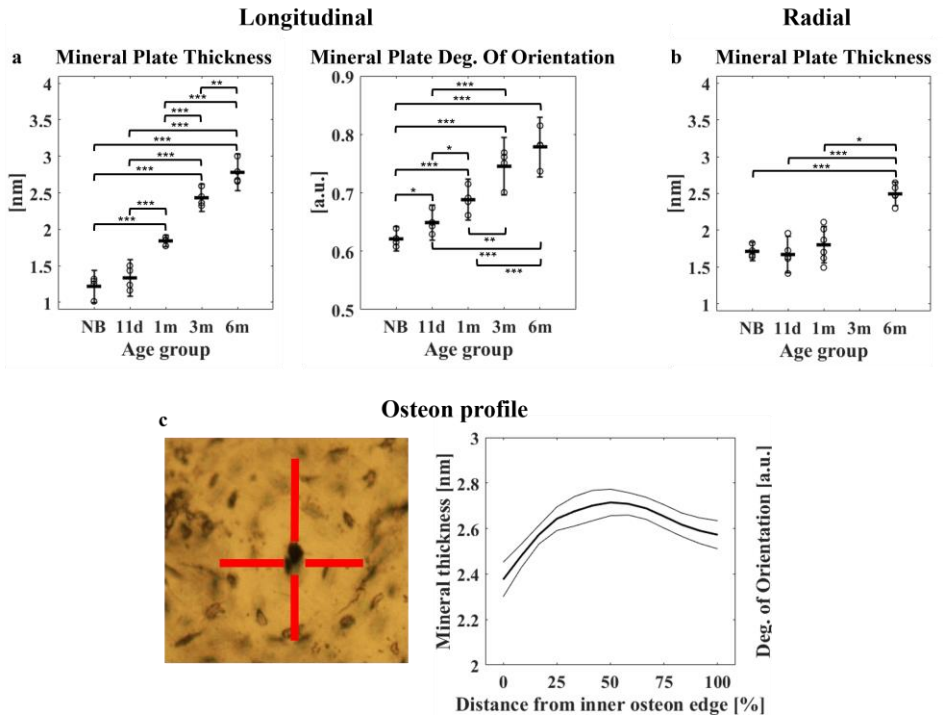


Figure 5.1. Main results from study I. Changes in mineral plate thickness and orientation, in longitudinal and radial sections, as a function of animal and tissue age. a) Changes in mineral plate thickness and degree of orientation with animal age for the longitudinal specimens. b) Changes in mineral plate thickness with animal age for the radial specimens. (c) Changes in mineral plate thickness as a function of tissue age (right), based on radial profiles in osteons (left).

Table 5.1. Pearson's linear correlation coefficients and corresponding p-values for comparison of specimen mean values of mineral plate thickness from study I and spectroscopic data obtained from the same specimens, published earlier in Turunen et al. (2011) [5].

| | FTIR | Raman |
|---|---|---|
| Crystallinity | R = -0.7, p = 0.6e-3 | R = 0.5, p = 3.8e-2 |
| Mineral/matrix | Not significant | R = 0.8, p = 5.0e-6 |
| Carbonate/phosphate | R = 0.8, p = 3.3e-6 | R = 0.6, p = 3.0e-3 |
| Carbonate/amide I | R = 0.8, p = 7.7e-6 | R = 0.9, p = 4.1e-7 |
| Acid phosphate substitution | R = -0.8, p = 2.5e-5 | N/A |

## 5.2 Comparison of SANS and SAXS (Study II)

SANS and SAXS data were acquired from cortical bone specimens, cut in perpendicular orientations (radial and longitudinal), obtained from three different species (cow, pig, and sheep). The integrated scattering intensities were compared in the overlapping $q$-range to elucidate similarities and differences between modalities. An order parameter, $S$, was used to quantify the orientational order of the mineral crystal plates.

The scattering data obtained with SANS was essentially identical to the corresponding SAXS data. Only minor differences ($\leq$ 15.4%) were seen when comparing the integrated scattering intensities in the overlapping q-region. These differences increased slightly as a function of $q$, with the SAXS intensity at higher $q$ being lower compared to the SANS intensity (Figure 5.2a, b). The orientational order, $S$, remained constant for both longitudinal and radial specimens in both SANS and SAXS ($S$ = 0.66 ± 0.09, and $S$ = 0.47 ± 0.14, mean ± std), for the longitudinal and the radial specimens, respectively (Figure 5.2c, d).

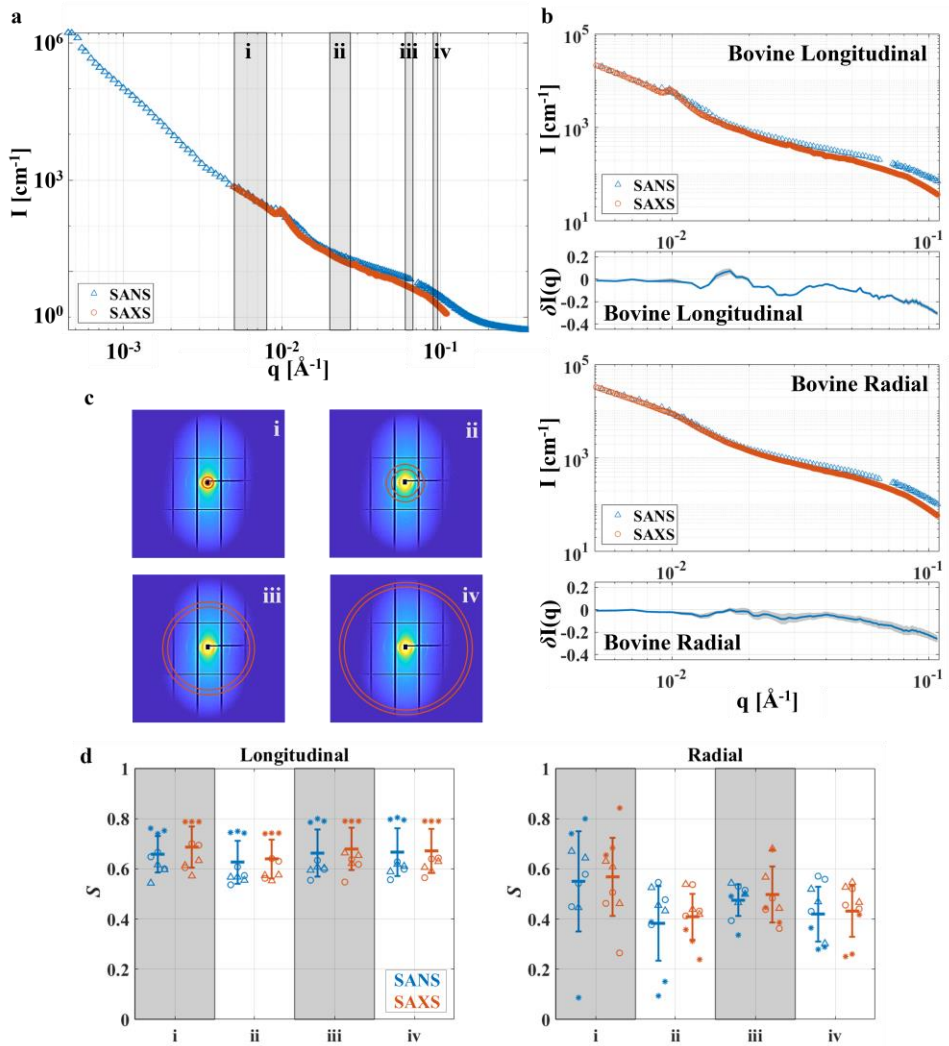


Figure 5.2. Main results from study II. Comparison of $I(q)$ in the overlapping $q$-range and of the structure parameter, $S$, at specific $q$-ranges. a) Representative $2\pi$ integration (log-log scale) of SANS (Δ) and SAXS (o) data from one measurement position on the longitudinal bovine specimen. The SAXS data was offset to overlap with the SANS data at low $q$. The $q$-ranges used for azimuthal integration (c, d) are indicated in grey. b) Zoom-in on the overlapping $q$-range for scattering data in (a). $q$-dependent intensity differences (linear-log scale) for full integration of SANS and SAXS scattering intensities in the overlapping $q$-region are shown below as mean (blue line) and standard deviation (shaded grey area) for the three measurement positions. c) 2D SAXS scattering patterns with overlays in red indicating the $q$-ranges used for the azimuthal integration (indicated in grey in (a)). d) $q$-range dependent order parameter ($S$), for longitudinal and radial specimens, shown as mean (thick horizontal lines) of SANS (blue) and SAXS (red) measurements, standard deviation (bar), and value per measurement position for bovine (Δ), porcine (o), and ovine (*).

## 5.3 Comparison of NT and XRT for visualising skeletal tissues (Study III)

Distal rat tibiae with metallic implants were imaged with NT and XRT. After superimposing the images using a dedicated image registration algorithm, the complementarity of the modalities was investigated by evaluating visualisation of different material phases (Figure 5.3a), by comparison of volume fractions in different locations in the specimen (Figure 5.3b), and by assessing the properties of the individual images, such as the CNR. The complementarity was further investigated via analysis of the dual modality histogram, joining the neutron and x-ray data. From these joint histograms, peaks with well-defined grey value intervals corresponding to the different material phases observed in the specimens were identified and compared.

Peak centre positions were different for all material phases (soft tissue, miscellaneous non-separated structures, high-density bone tissue, and metallic implant) in both NT and XRT, whilst only the peak corresponding to miscellaneous non-sorted structures had different centre positions in XRT for the two treatment groups. AUC/TA for the peak corresponding to soft tissue was higher in the Ctrl group than in the Trtd group. CNR revealed that for both bone and soft tissues, NT gave a higher contrast against the background than XRT. For the implant, the opposite was observed. Significantly more bone was measured around the implant (ROI 1) in the Trtd than in the Ctrl group both for NT and XRT (Figure 5.3c). No statistically significant differences were found between the measurements from the two imaging modalities. The phase segmentation did not show differences between the treatment groups. All three segmentations resulted in similar volume fractions for the high-density bone tissue in the ROI distal to the implant (ROI2, Figure 5.3d). Segmentation of soft tissue in the metaphysis (ROI 3) resulted in similar volume fractions for NT and the phase segmentation (PS), whereas it was higher with XRT (Figure 5.3e). Bone volume fractions in the metaphysis were similar for NT and XRT, but lower for the PS.

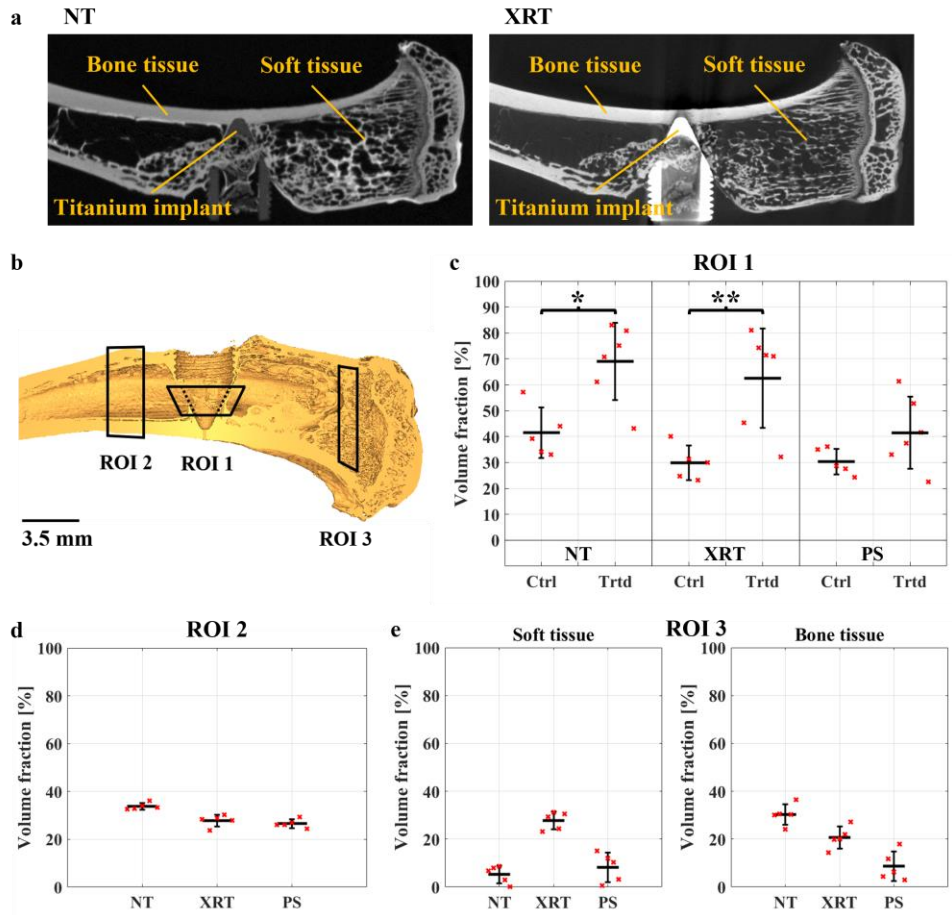


Figure 5.3. Main results from study III. Visualisation of material phases for NT and XRT, and comparison of volume fractions of bone tissue and soft tissue segmented using thresholding of NT and XRT, and phase segmentation (PS). a) Midline sagittal slices of registered NT and XRT images for a representative specimen from the Trtd group. Material phases are indicated in orange. b) Midline sagittal slice through a volume rendering of the segmented bone phase (based thresholding) in the NT image of a representative specimen from the Ctrl group. The three ROIs used to quantify peri-implant bone (ROI 1), cortical bone (ROI 2), and soft tissue and trabecular bone (ROI 3) are indicated in black. c) Volume fractions of peri-implant bone tissue (ROI 1). Statistically significant differences are indicated with * ($p < 0.05$) and ** ($p < 0.01$). d) Volume fractions of high-density bone tissue in the distal shaft in specimens from the Ctrl group (ROI 2). e). Volume fractions of soft tissue and bone tissue in the metaphysis in specimens from the Ctrl group (ROI 3).

## 5.4 Effects of hydration state on NT images of bone (Study IV)

Distal rat tibiae and trabecular bovine bone plugs were imaged with NT at different hydration states, to elucidate the effects on contrast between material phases. Contrast was evaluated based on CNR, line profiles, and image histograms. To account for changes in mechanical properties due to drying and rehydration, the trabecular bone plugs were tested in unconfined uniaxial compression and mechanical properties (peak stress, Young's modulus, and toughness) were compared between hydration groups.

CNR for cortex vs background decreased with increasing hydration (Figure 5.4c). After rehydration for > 40 h, free $D_2O$ was seen in the intramedullary canal (Figure 5.4a). At this time point, CNR between bone tissue and $D_2O$, and between background and $D_2O$, was lower than between bone tissue and background. The line profiles showed decreased contrast (difference in grey value intensity) between cortex and background with increasing rehydration (Figure 5.4b). When the intramedullary canal was filled with $D_2O$, contrast was only seen between $D_2O$ and soft tissue. In addition, thickening of the cortex as the tissue was rehydrated was observed. The histograms of the trabecular bone plugs displayed peaks corresponding to void, bone tissue, and marrow (Figure 5.4e). The soaked specimens lacked the peak corresponding to void, except for in one specimen. The dried specimens had prominent void peaks and displayed a merging of the peaks corresponding to bone tissue and marrow. The low contrast between these two phases was evident also by visual inspection of the tomographic images of the dried specimens (Figure 5.4d). The rehydrated specimens had separated bone tissue and marrow peaks but also exhibited void peaks. The linear mixed-effects analysis used to assess the mechanical properties obtained from the compression test of the trabecular bone plugs showed no differences between hydration states, indicating that drying for 3 h does not substantially affect the mechanical properties of these types of specimens.

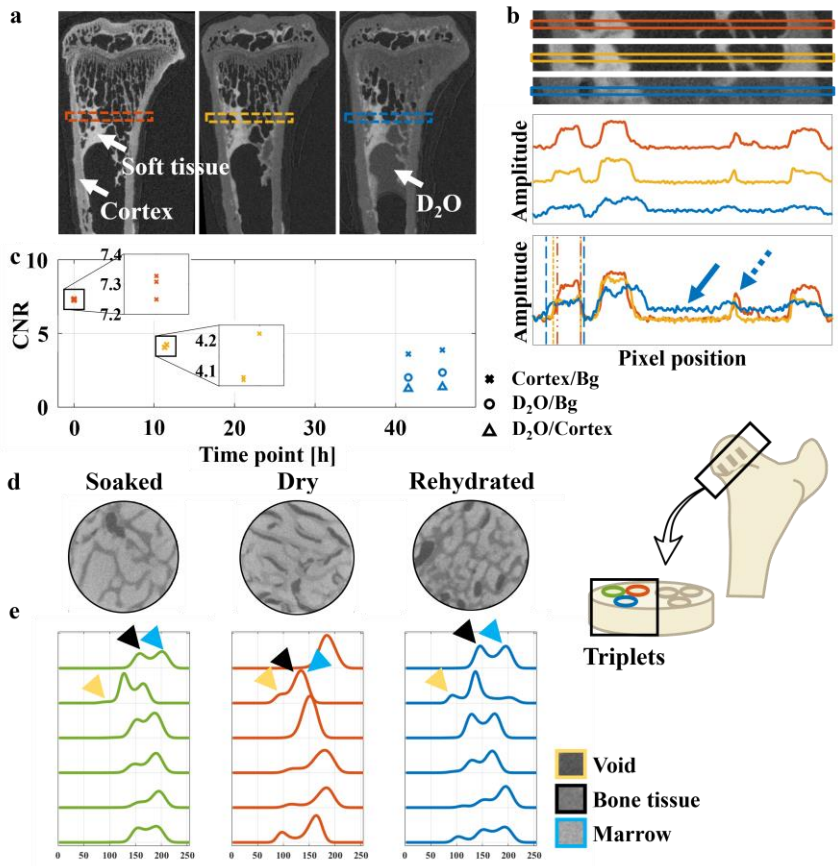


Figure 5.4 Main results from study IV. Contrast between material phases at different hydration states for rat tibiae and trabecular bovine bone plugs. a) Sagittal slices of a rat tibia with regions for line profile indicated with dashed square; dried (red), rehydrated 12 h (orange), rehydrated > 40 h (blue). Bone cortex, soft tissue, and $D_2O$ are indicated with white arrows. b) Zoom-in of the regions in (a), with corresponding separated and overlaid line profiles. Thickening of the cortex with increased hydration is indicated with dashed lines. The arrows indicate increased signal due to $D_2O$ (solid), and reduced contrast for inner structures (dashed). c) CNR for cortex vs background (Bg), $D_2O$ vs Bg, and $D_2O$ vs cortex at the different hydration states, with zoom-ins of the first two hydration states for easier identification of the individual data points. d) Transverse slices of representative trabecular bovine bone plug specimens from each hydration group. e) Specimen-specific histograms. Each row corresponds to one triplet, i.e., plugs extracted next to each other from the same anatomical location. Arrows indicate peaks corresponding to void (yellow), bone tissue (black), and marrow (blue).

# 6. Discussion

## 6.1 General

The aim of this thesis was to investigate the possible complementarity of selected neutron and x-ray techniques for structural characterisation of skeletal tissues at different length scales. In studies I and II, SAS was used to characterise the nanostructure, namely the thickness and organisation of the HAp mineral plates, and to elucidate the possibilities of obtaining structural information about the collagen matrix using SANS. In studies III and IV, tomography was used to visualise the microstructure. Study III focussed on the complementarity of NT and XRT. In Study IV, the effects of hydration state on neutron tomographic images were explored.

The two techniques, i.e., SAS and tomography, were chosen since they target length scales that are important for answering questions about how bone structure relates to the mechanical integrity of bone tissue. SAS probes the nanoscale, where the amount, size, and alignment of the mineral phase affects fracture resistance. A better understanding of the interplay between changes in bone nanostructure and damage resistance enables, e.g., development of drugs and other medical interventions for correction of deviations from a healthy nanostructure. Tomography has several applications but the focus in this thesis was on microstructural characterisation with the aim of assessing bone-implant integration. Surgical revisions due to implant loosening are costly and cause excess suffering for the patient. A better understanding of damage mechanisms leading to failed implant anchorage makes it possible to improve implant designs and develop medical treatments to improve implant stability.

Although x-rays are state-of-the-art in bone research in general, and for SAS and tomography specifically, they are not always ideal for structural characterisation of bone tissue. As has been shown in this thesis, neutrons are complementary to x-rays and can help tackle some of the challenges associated with x-rays in bone research. However, there are also challenges that must be addressed with neutrons. Some of these were highlighted through the studies in this thesis and will be discussed in the following sections.

## 6.2 Small-angle scattering

The high flux and small spot size of synchrotron based SAXS measurements enables mapping of large areas at high resolution (see e.g., Figure 6.1b). This is a powerful tool as it facilitates collection of large datasets, which is of high importance when studying biological system where the intra- and inter-variability within and between specimens can be large. Study I was designed to gain insight into how the mineral phase in bone changes during maturation and growth. To this end, perpendicular cortical bone sections (Figure 6.1a) were obtained from young New Zealand White rabbits at different stages of maturation. One of the findings was that the thickness of the mineral plates differed between the longitudinal and radial sections. Previous studies have suggested the presence of at least two different types of mineral populations, with differing orientations and size [27,32,33]. This notion is supported by a more recent study by Grünewald et al. (2020), where SAXS and WAXS tensor tomography of human bone indicated two differently oriented mineral populations [73]. The initial hypothesis regarding the discrepancies in thickness between longitudinal and radial sections was that these apatite morphologies were visualised differently in the different sections. Upon further consideration, this hypothesis may need to be revised. For there to be differences in size between sections, one morphology would have to be more prevalent in one section than the other and vice versa. The fitting method used to calculate the thickness includes an assumption on size distribution [38]. Assuming that (1) the model is correct, so that the predicted thickness represents the thickness of the mineral plates, and that (2) the size distribution is reasonable, the model gives a thickness that is the actual average thickness. Both assumptions are backed up by the fit to the data and with results from other studies in literature. Hence, the data in study I indicates that thicker mineral plates were more prevalent in the longitudinal sections, whilst thinner mineral plates were more prevalent in the radial sections. However, as the specimens were obtained from the same cohort and all data were treated in the same way, there are no apparent reasons for the discrepancy. Further investigation would be warranted to elucidate the underlying cause.

One limitation in study I was regarding the analysis of changes with tissue age. Osteonal structures were identified in specimens from the age of 1 month using light microscopy. However, the regions measured with SAXS could only be positively identified in one of the specimens in the oldest age group. In this specimen, five osteons were selected, and four radial profiles were obtained from each osteon. Since only a small number of osteons were investigated, the evolution of mineral plate thickness and organisation as a function of tissue age cannot be considered conclusive, only indicative.

The initial plan was to measure the specimens from study I with SANS. However, measurements at the D11 beamline at ILL, Grenoble, France [144] pointed to that the dimensions of the young rabbit were too small. Instead, study II was set up to compare SANS and SAXS measurements on bone specimens from mature animals with bones of larger dimensions. To elucidate the similarities between SANS and SAXS, specimens were obtained from different species and with different microstructural orientation. Comparison of the SANS and SAXS data revealed striking similarities between the datasets and the results from the study demonstrate that SANS yields the same structural information as SAXS. The slight discrepancies seen could be attributed to uncertainties in the background subtraction, as an over-subtraction in the SAXS data would explain the increase in difference at high $q$.

During the SANS experiment, attempts were made to collect data using a Ø 0.5 mm beam spot size. However, the intensity of the signal proved to be ~1 order of magnitude lower than when using a beam spot size of Ø 2 mm. Furthermore, comparing the scattering data acquired using the two different spot sizes showed no apparent differences in distinguished features. Hence, it was decided to use the larger spot size for the ultimate data collection for the study (Figure 6.1c). An attempt at contrast matching was also done and short (5 min) measurements were performed on one specimen immersed in 82% $D_2O$:$H_2O$ (matched to the collagen) and on one specimen immersed in 39% $D_2O$:$H_2O$ (matched to the mineral). Comparison of the data showed no differences in curve features but only differences in intensity that was assumed to come from non-uniform thickness of the specimens. Although no definitive conclusions can be drawn based on such short measurement times, the similarity of the scattering curves indicates that the amount of water in cortical bone is not enough for contrast matching to be successful.

One limitation in study II was the differences in beam dimensions between the SANS and SAXS measurements. Although this was in part accounted for by scanning larger areas with SAXS and averaging the acquired scattering data, the measured volumes differed (3.14 $mm^3$ and 1.35 $mm^3$ for SANS and SAXS, respectively). However, the XRT data showed that the microstructure inside the measured volumes was homogeneous. Since the scattering signal is an average over all scattering structures in the measured volume, heterogeneity in the sample equates to smearing of the scattering data. As the volumes were relatively large, minor structural discrepancies should not have a noticeable effect on the resulting scattering data due to the averaging. Moreover, the resolution of the SANS and SAXS measurements differed, with that of SAXS being considerably higher than for SANS [142,144]. Nevertheless, as the polydispersity of the mineral platelets is relatively high [31], the shape of the scattering curves could be explained by the polydispersity rather than the wavelength distribution. In fact, the lower resolution of the SANS data further explains the differences in intensity seen around the collagen peaks and thereby indicated that even larger similarities between the two modalities could have been seen if the resolutions had been

more similar. Finally, the specimens were stored in ethanol and measured in air. This resulted in drying of the tissue. Drying and ethanol fixation of non-mineralised tissue is known to affect the collagen [147,152]. However, changes due to dehydration on mineralised tissue are less prominent [43]. Since both SANS and SAXS measurements were carried out in the same fashion, the degree of dehydration and potential change to the collagen organisation should be the same for both. Furthermore, as the specimens were not dried prior to fixation in ethanol, and due to the solvent being 70%, enough water remained in the tissue for there to have been a possible contribution to the scattering pattern.

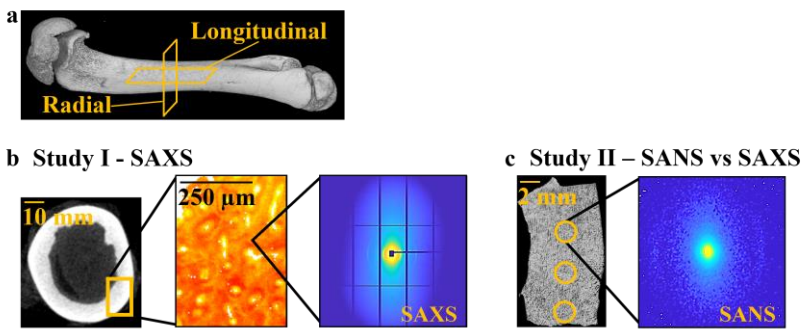


Figure 6.1. SAS from cortical bone. a) In both study I and II perpendicular sections of cortical bone from the mid-diaphysis of long bones were used. b) Study I employed scanning SAXS to map regions of the specimens (left) at high-resolution. Due to the small beam spot size (5.5×4 µm$^2$), the scattering maps (middle) achieved a pixel size of 5×5 µm$^2$, with each pixel corresponded to one 2D scattering pattern (right). c) Study II employed SANS and SAXS to compare the scattering signal between the modalities. Three positions with dimensions dictated by the SANS beam spot size (Ø 2 mm) were investigate on each specimen (left). For SANS, each position yielded one 2D scattering pattern (right). For SAXS, scans were done to map a region with similar size to that covered by the SANS measurement.

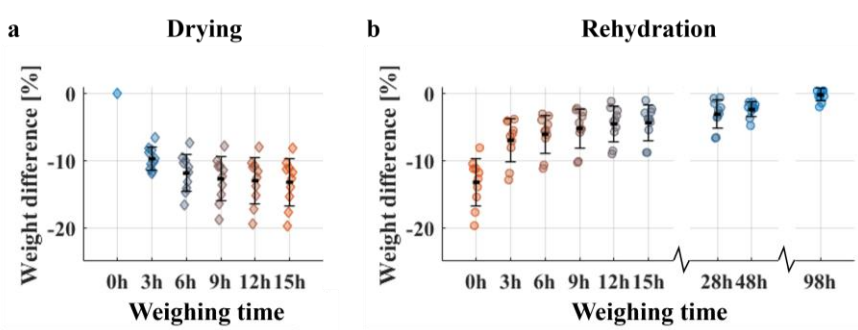


Figure 6.2. Weight changes due to drying and rehydration of trabecular bovine bone plugs used in study IV. a) Weight difference compared to original weight during drying. b) Weight difference compared to original weight (before drying) during rehydration.

## 6.3 Tomographic imaging

The initial plan for the thesis work included performing in-situ implant pull-out experiment during NT, to follow up earlier studies [23,24]. However, during an experiment at the NeXT-Grenoble beamline at ILL, France, the first images displayed insufficient visibility of internal structures due to the hydration state of the specimens. Hence, for study III the specimens were dried, and the focus was instead turned towards elucidating similarities and differences in what structures and material phases could be visualised with NT and XRT. Comparison of the modalities was in part performed by analysis of the joint histogram, joining the grey value distributions of both image sets. Most of the data analysis was carried out during a research stay at Laboratoire 3SR in Grenoble, France, where the research group developing the dual modality image registration algorithm employed to compare the NT and XRT datasets resides [151]. As this was the first application of the algorithm on bone samples, augmentation of the registration approach was done in collaboration with the 3SR researchers. However, further improvements could be made. The quality of the phase segmentation could possibly be enhanced by increasing the resolution of the joint histogram and phase map used for the registration. However, this would come with increased computational cost. For the registration of the full-size (not down-sampled) images used in the study (~1 GB per image volume), the computations needed to be performed on the Aurora cluster on LUNARC. Nevertheless, further exploration of the possibilities of joining NT and XRT data in this manner could result in a novel way of identifying tissues and their distribution in the specimens.

Study IV was devised to address the issues with insufficient visibility of internal structures encountered in study II and in Le Cann et al. (2017) [24]. In Le Cann et al. (2017), a protocol was adopted to exchange $H_2O$ for $D_2O$ by soaking the specimens in $D_2O$ for 3 days prior to imaging, in an attempt at reducing the obscuring effects of the hydrogen. They experienced difficulties with one of their specimens and attributed it to over-hydration with $D_2O$. However, it was subsequently suspected that there had not been sufficient exchange of $H_2O$ for $D_2O$ in that specimen. Therefore, the same exchange protocol was applied to the specimens in study III. When the first neutron images showed low visibility of internal structures, the hypothesis changed to that exchange by diffusion was not sufficient for exchange of $H_2O$ for $D_2O$. Consequently, the new exchange protocol used in study IV was designed to remove $H_2O$ before replenishing the tissue with $D_2O$. However, the conclusion in study IV was that the amount of free liquid in the specimen, regardless of hydrogen isotope, is what affects the visibility of structures. This poses some challenges. How can this free water be removed? Drying works to this objective. However, the effects on the mechanical properties remain to be fully elucidated. Drying of bone has been shown to increase stiffness and brittleness [137–140,153]. Yet, the compression tests of the trabecular bovine bone plugs in study IV provided results that contradict this. No changes to the mechanical properties due to neither drying nor rehydration were

seen in the study. From the analysis of the grey value distributions in the NT images of the bone plugs, it was seen that there was reduced contrast between bone and marrow after drying, as compared to in the groups that were soaked or rehydrated in salinated $D_2O$. This shows that the duration used for the drying (3 h) yields adequate extraction of $H_2O$ for there to be an impact on how neutrons interact with the tissue. Drying of an additional 10 trabecular bone plugs for 15 h, weighing every 3 h, showed that most water content was indeed lost during the first 3 h (Figure 6.2a), with weights of the specimens decreasing with 9.7% ± 1.7% in that timeframe. The duration for rehydration (and soaking in the control group) was chosen to match the exchange protocol used in Le Cann et al. (2017) [24]. Furthermore, full rehydration was expected to have occurred after 3 h [139]. However, the bone plugs were found to have a lower weight after 48 h of rehydration than in their original state. Rehydration of the 10 additional bone plugs used to evaluate the weight loss during drying showed that 48.9% ± 9.9% of the lost weight was regained after 3 h and 81.9% ± 5.3% after 48 h (Figure 6.2b). The experiment also showed that almost all weight changes were reversed by rehydrating for another 50 h. However, as no differences in mechanical properties were observed between the soaked and rehydrated groups, prolonging the rehydration duration appears unnecessary. For the rat tibiae, it was seen that rehydration for > 40 h did not fully bring the specimens back to their original weight, yet still caused free water to accumulate in the intramedullary canal. The sectioning of the rat tibiae left the intramedullary canal exposed and made infiltration of liquid easier. Sectioning of the specimens has so far been required due to the experimental setups for implant pull-out, where the tibiae have been placed with the long axis parallel with the horizontal plane. As the distance between a sample and the detector should be minimised to reduce image blur, sectioning has been necessary. One could imagine a different setup where the tibiae were mounted vertically, as in the tomographic studies presented in this thesis. This would remove the requirement of sectioning as the distal parts could simply be placed outside of the FOV. However, although such a setup is feasible design-wise, it would likely come at the cost of increased sample-detector distance, as the implant should be at the centre of the rotational axis for optimal depicture in the images. Assuming sectioning is necessary, closing the opening to the intramedullary canal using some sort of plugging material after drying the specimen could be an option for stopping liquid from entering. Another option would be to device a method for removing the liquid, e.g., by suction. It is difficult to know how successful such a method would be, as much of the intramedullary canal could be filled with peri-implant bone that would complicate access. Nevertheless, if such a solution could be realised, it would make it so that drying of the specimens would not be necessary, as any interstitial fluid would be removable mechanically.

## 6.4 Future perspectives

Two different techniques, namely SAS and tomography, were employed for structural characterisation of bone tissue in this thesis, with focus on evaluating the possibilities of using neutrons in each technique. Based on the conclusions drawn herein, the future perspectives of the applicability of neutrons in the two techniques vary.

SAXS is a powerful tool for investigating bone nanostructure and is already widely used. As shown in this thesis, SANS does not yield any apparent additional information about bone nanostructure for the kind of bone samples investigated here as they, effectively, contain only two scattering components – collagen and mineral. Although SANS provides equivalent scattering patterns to SAXS, the lower resolution and longer measurements times make SANS less suitable for studying cortical bone nanostructure. However, its place in musculoskeletal tissue research overall is not yet fully elucidated as it might be beneficial for studying other hard or soft tissues.

Neutrons for microstructural characterisation through tomography is a promising complement to x-rays. As shown in study III and in Guillaume et al. (2021) [25], the interaction between neutrons and soft skeletal tissues creates good contrast against other material phases. Soft tissue distribution is, e.g., an indicator for bone remodelling during bone-implant integration [99]. In Raina et al. (2019) [99], soft tissue was visualised by means of histology. This is a common way of distinguishing between soft and hard skeletal tissues as different stains can bring out different tissue types [99,154]. However, histology is an inherently destructive technique that yields only 2D maps of tissue distribution. NT brings the added value compared to XRT and histology of not only enabling visualisation of bone tissue but also bone marrow and other soft skeletal tissues in 3D. Other imaging techniques exist that can be used to the same end. Dual energy computed tomography (DECT) is an x-ray based technique used clinically to visualise soft musculoskeletal tissues [155,156]. DECT has also been used in research of, e.g., concrete and stained mouse organs [157,158], and improved instrumentation is bringing the spatial resolution down to a few micrometres [159]. Comparing the capabilities of NT and DECT for soft tissue differentiation could be a next step in evaluating the capabilities of NT.

Both spatial and temporal resolution in NT are limited in comparison to XRT. Technological advances regarding, e.g., detector systems aid in improving both. Still, flux remains as the main limiting factor. When the ESS comes online, this limit will be pushed and the applicability of NT will improve. However, NT acquisition times are currently down to the second range [58], and resolution is approaching 4 µm [84,85]. The improved speed is especially exciting as it allows for in-situ mechanical tests at a physiologically more relevant speed than has previously been possible [24]. Still, the issue with limited visibility due to over-hydration needs to be addressed before in-situ mechanical testing can commence.

# 7. Summary and conclusions

The overall aim of this thesis was to investigate the possibilities of using neutron scattering techniques as a complement or alternative to x-rays for studying bone tissue structure on different length scales. Small-angle scattering for nanostructural characterisation and tomography for microstructural characterisation were chosen for comparison between modalities. Situations and conditions where neutrons could be preferable to x-rays were identified by comparing pros and cons of the respective techniques.

Below, the main conclusions of each study (I-IV) are summarised.

I. *The mineral plates in bone grow in thickness and become more organised during maturation and growth.* Cortical bone sections from New Zealand White rabbits at different stages of maturation were scanned with SAXS and curve fitting was used to obtain nanostructural parameters from the scattering data. The resulting maps of scattering parameters showed that the thickness of the mineral plates increase, and their alignment becomes more homogeneous with age.

II. *SANS and SAXS from cortical bone show highly similar scattering patterns.* Cortical bone sections from different species were investigated with SANS and SAXS. Comparison of the scattering data revealed effectively identical scattering patterns. This strongly points to that bone, at the nanoscale, can be seen as a biphasic material in the analysis of scattering data for structural characterisation, with effective contrast between the organic collagen matrix and the inorganic mineral plates.

III. *NT and XRT are highly complementary modalities for visualising bone microstructure.* Proximal rat tibiae with titanium implants were imaged with NT and XRT and distinguishability of the microstructure was compared between modalities. Visualisation of bone tissue was similar for the modalities, but NT has the added value of circumventing metal image artefacts and the benefit of highlighting soft tissue.

IV. *Visibility of microstructures in NT images is affected by the hydration levels of the tissue.* NT images were acquired of bone specimens at different hydration states and visibility of internal structures was assessed. The analysis showed that presence of free water inside the specimens caused detrimentally reduced contrast between bone and surrounding structures.

# 8. References


1. Reznikov, N., Shahar, R. & Weiner, S. Bone hierarchical structure in three dimensions. *Acta Biomater.* 10, 3815–3826 (2014) doi:10.1016/j.actbio.2014.05.024.
2. Rho, J.-Y., Kuhn-Spearing, L. & Zioupos, P. Mechanical properties and the hierarchical structure of bone. *Med. Eng. Phys.* 20, 92–102 (1998) doi:10.1016/S1350-4533(98)00007-1.
3. van der Linden, J. C. & Weinans, H. Effects of microarchitecture on bone strength. *Curr. Osteoporos. Rep.* 5, 56–61 (2007) doi:10.1007/s11914-007-0003-3.
4. Isaksson, H., Harjula, T., Koistinen, A., Iivarinen, J., Seppänen, K., Arokoski, J. P. A., *et al.* Collagen and mineral deposition in rabbit cortical bone during maturation and growth: Effects on tissue properties. *J. Orthop. Res.* 28, 1626–1633 (2010) doi:10.1002/jor.21186.
5. Turunen, M. J., Saarakkala, S., Rieppo, L., Helminen, H. J., Jurvelin, J. S. & Isaksson, H. Comparison between Infrared and Raman Spectroscopic Analysis of Maturing Rabbit Cortical Bone. *Appl. Spectrosc.* 65, 595–603 (2011) doi:10.1366/10-06193.
6. Turunen, M. J., Saarakkala, S., Helminen, H. J., Jurvelin, J. S. & Isaksson, H. Age-related changes in organization and content of the collagen matrix in rabbit cortical bone. *J. Orthop. Res.* 30, 435–442 (2012) doi:10.1002/jor.21538.
7. Fratzl, P., Fratzl-Zelman, N., Klaushofer, K., Vogl, G. & Koller, K. Nucleation and growth of mineral crystals in bone studied by small-angle X-ray scattering. *Calcif. Tissue Int.* 48, 407–413 (1991) doi:10.1007/BF02556454.
8. Burger, C., Zhou, H., Wang, H., Sics, I., Hsiao, B. S., Chu, B., *et al.* Lateral packing of mineral crystals in bone collagen fibrils. *Biophys. J.* 95, 1985–1992 (2008) doi:10.1529/biophysj.107.128355.
9. Legros, R., Balmain, N. & Bonel, G. Age-related changes in mineral of rat and bovine cortical bone. *Calcif. Tissue Int.* 41, 137–144 (1987) doi:10.1007/BF02563793.
10. Ferretti, J. Bone mass, bone strength, muscle–bone interactions, osteopenias and osteoporoses. *Mech. Ageing Dev.* 124, 269–279 (2003)

doi:10.1016/S0047-6374(02)00194-X.

11. Fratzl, P. & Weinkamer, R. Nature's hierarchical materials. *Prog. Mater. Sci.* 52, 1263–1334 (2007) doi:10.1016/j.pmatsci.2007.06.001.

12. Batdehmbehrehl, G., Chultehm, D. & Sangaa, D. An investigation of fossil bone mineral structure with neutron scattering (JINR-R--14-99-131). *Joint Institute for Nuclear Research* (1999).

13. Chappard, C., Menelle, A. & Daudon, M. 482 Analysis of hydroxyapatite subchondral bone in osteoarthritis of the hip by Fourier transform infrared and powder neutron diffraction methods. *Osteoarthr. Cartil.* 18, S217 (2010) doi:10.1016/S1063-4584(10)60511-0.

14. Chappard, C., André, G., Daudon, M. & Bazin, D. Analysis of hydroxyapatite crystallites in subchondral bone by Fourier transform infrared spectroscopy and powder neutron diffraction methods. *Comptes Rendus Chim.* 19, 1625–1630 (2016) doi:10.1016/j.crci.2015.03.015.

15. Benmarouane, A., Citterio-Bigot, H., Geandier, G., Hansen, T., Millet, P. & Lodini, A. Synchrotron radiation and neutron diffraction study of hydroxyapatite in bone at the interface with implant. *Mater. Sci. Forum* 748–753 (2010) doi:10.4028/www.scientific.net/MSF.638-642.748.

16. Benmarouane, A., Hansen, T., Millet, P., Lambotte, J. C. & Lodini, A. Spatially resolved texture investigations of the rabbit bone-implant interface by neutron diffraction. *J. Neutron Res.* 12, 123–127 (2004) doi:10.1080/10238160410001734568.

17. Benmarouane, A., Hansen, T., Millet, P. & Lodini, A. Investigation of the hydroxyapatite crystallites in bone at the interface with implant by neutron diffraction. *Mater. Sci. Forum* 612–616 (2007) doi:10.4028/www.scientific.net/MSF.539-543.612.

18. Bonar, L. C., Lees, S. & Mook, H. A. Neutron diffraction studies of collagen in fully mineralized bone. *J. Mol. Biol.* 181, 265–270 (1985) doi:10.1016/0022-2836(85)90090-7.

19. Skakle, J. M. S. & Aspden, R. M. Neutron diffraction studies of collagen in human cancellous bone. *J. Appl. Crystallogr.* 35, 506–508 (2002) doi:10.1107/S002188980200972X.

20. Lees, S., Barnard, S. M. & Mook, H. A. Neutron studies of collagen in lathyritic bone. *Int. J. Biol. Macromol.* 9, 32–38 (1987) doi:10.1016/0141-8130(87)90022-5.

21. Lees, S., Capel, M., Hukins, D. W. L. & Mook, H. A. Effect of sodium chloride solutions on mineralized and unmineralized turkey leg tendon. *Calcif. Tissue Int.* 61, 74–76 (1997) doi:10.1007/s002239900298.

22. Lees, S., Bonar, L. C. & Mook, H. A. A study of dense mineralized tissue by neutron diffraction. *Int. J. Biol. Macromol.* 6, 321–326 (1984)

doi:10.1016/0141-8130(84)90017-5.

23. Isaksson, H., Le Cann, S., Perdikouri, C., Turunen, M. J., Kaestner, A., Tägil, M., *et al.* Neutron tomographic imaging of bone-implant interface: Comparison with X-ray tomography. *Bone* 103, 295–301 (2017) doi:10.1016/j.bone.2017.07.022.

24. Le Cann, S., Tudisco, E., Perdikouri, C., Belfrage, O., Kaestner, A., Hall, S., *et al.* Characterization of the bone-metal implant interface by Digital Volume Correlation of in-situ loading using neutron tomography. *J. Mech. Behav. Biomed. Mater.* 75, 271–278 (2017) doi:10.1016/j.jmbbm.2017.07.001.

25. Guillaume, F., Le Cann, S., Tengattini, A., Törnquist, E., Falentin-Daudre, C., Albini Lomami, H., *et al.* Neutron microtomography to investigate the bone-implant interface – comparison with histological analysis. *Phys. Med. Biol.* 66, 105006 (2021) doi:10.1088/1361-6560/abf603.

26. Törnquist, E., Le Cann, S., Tudisco, E., Tengattini, A., Andò, E., Lenoir, N., *et al.* Dual modality neutron and x-ray tomography for enhanced image analysis of the bone-metal interface. *Phys. Med. Biol.* 66, 135016 (2021) doi:10.1088/1361-6560/ac02d4.

27. Rindby, A., Voglis, P. & Engström, P. Microdiffraction studies of bone tissues using synchrotron radiation. *Biomaterials* 19, 2083–2090 (1998) doi:10.1016/S0142-9612(98)00120-3.

28. Stock, S. R. The mineral–collagen interface in bone. *Calcif. Tissue Int.* 97, 262–280 (2015) doi:10.1007/s00223-015-9984-6.

29. Bala, Y., Farlay, D. & Boivin, G. Bone mineralization: from tissue to crystal in normal and pathological contexts. *Osteoporos. Int.* 24, 2153–2166 (2013) doi:10.1007/s00198-012-2228-y.

30. Fratzl, P., Schreiber, S. & Boyde, A. Characterization of bone mineral crystals in horse radius by small-angle x-ray scattering. *Calcif. Tissue Int.* 58, 341–346 (1996) doi:10.1007/s002239900056.

31. Døvling Kaspersen, J., Turunen, M. J., Mathavan, N., Lages, S., Skov Pedersen, J., Olsson, U., *et al.* Small-angle x-ray scattering demonstrates similar nanostructure in cortical bone from young adult animals of different species. *Calcif. Tissue Int.* 99, 76–87 (2016) doi:10.1007/s00223-016-0120-z.

32. Lees, S. A model for the distribution of HAP crystallites in bone—an hypothesis. *Calcif. Tissue Int.* 27, 53–56 (1979) doi:10.1007/BF02441161.

33. Danilchenko, S., Kalinkevich, A., Zhovner, M., Kuznetsov, V., Li, H. & Wang, J. Anisotropic aspects of solubility behavior in the demineralization of cortical bone revealed by XRD analysis. *J. Biol. Phys.*

45, 77–88 (2019) doi:10.1007/s10867-018-9516-5.

34. Törnquist, E., Isaksson, H. & Turunen, M. J. Mineralization of cortical bone during maturation and growth in rabbits. *J. Bone Miner. Metab.* 38, 289–298 (2020) doi:10.1007/s00774-019-01068-y.

35. Reznikov, N., Bilton, M., Lari, L., Stevens, M. M. & Kröger, R. Fractal-like hierarchical organization of bone begins at the nanoscale. *Science (80-. ).* 360, 507–518 (2018) doi:10.1126/science.aao2189.

36. Fratzl, P. & Paris, O. Complex biological structures: collagen and bone. in *Neutron scattering in biology* 205–223 (Springer, Berlin, Heidelberg, 2006). doi:10.1007/3-540-29111-3_11.

37. Turunen, M. J., Døvling Kaspersen, J., Olsson, U., Guizar-Sicairos, M., Bech, M., Schaff, F., *et al.* Bone mineral crystal size and organization vary across mature rat bone cortex. *J. Struct. Biol.* 195, 337–344 (2016) doi:10.1016/j.jsb.2016.07.005.

38. Bünger, M. H., Oxlund, H., Hansen, T. K., Sørensen, S., Bibby, B. M., Thomsen, J. S., *et al.* Strontium and bone nanostructure in normal and ovariectomized rats investigated by scanning small-angle x-ray scattering. *Calcif. Tissue Int.* 86, 294–306 (2010) doi:10.1007/s00223-010-9341-8.

39. Camacho, N. P., Rinnerthaler, S., Paschalis, E. P., Mendelsohn, R., Boskey, A. L. & Fratzl, P. Complementary information on bone ultrastructure from scanning small angle X-ray scattering and Fourier-transform infrared microspectroscopy. *Bone* 25, 287–293 (1999) doi:10.1016/S8756-3282(99)00165-9.

40. Fratzl, P., Gupta, H. S., Paschalis, E. P. & Roschger, P. Structure and mechanical quality of the collagen-mineral nano-composite in bone. *J. Mater. Chem.* 14, 2115–2123 (2004) doi:10.1039/B402005G.

41. Weiner, S. & Traub, W. Bone structure : from ångström to microns. *J. FASEB* 6, 879–885 (1992).

42. Isaksson, H., Malkiewicz, M., Nowak, R., Helminen, H. J. & Jurvelin, J. S. Rabbit cortical bone tissue increases its elastic stiffness but becomes less viscoelastic with age. *Bone* 47, 1030–1038 (2010) doi:10.1016/j.bone.2010.08.015.

43. Unal, M., Yang, S. & Akkus, O. Molecular spectroscopic identification of the water compartments in bone. *Bone* 67, 228–236 (2014) doi:10.1016/j.bone.2014.07.021.

44. Granke, M., Does, M. D. & Nyman, J. S. The role of water compartments in the material properties of cortical bone. *Calcif. Tissue Int.* 97, 292–307 (2015) doi:10.1007/s00223-015-9977-5.

45. Wolff, J. Ueber die innere Architectur der Knochen und ihre Bedeutung für die Frage vom Knochenwachsthum. *Arch. für Pathol. Anat. und*

*Physiol. und für Klin. Med.* 50, 389–450 (1870) doi:10.1007/BF01944490.

46. Amprino, R. & Engstrom, A. Studies on x-ray absorption and diffraction of bone tissue. *Acta Anat. (Basel).* 15, 1–22 (1952).

47. Neutron imaging and applications - A reference for the imaging community. (eds. Bilheux, H. Z., McGreevy, R. & Anderson, I. S.) (Springer US, 2009). doi:10.1007/978-0-387-78693-3.

48. Hoogerheide, D. P., Forsyth, V. T. & Brown, K. A. Neutron scattering for structural biology. *Phys. Today* 73, 36–42 (2020) doi:10.1063/PT.3.4498.

49. Kostorz, G. & Lovesey, S. W. Neutron scattering - General introduction. in *Treatise on Materials Science and Technology* vol. 15 1–67 (Academic Press, Inc., 1979). doi:10.1016/B978-0-12-341815-9.50009-4.

50. Hsieh, J. Chapter 2 - Preliminaries. in *Computed Tomography: Principles, Design, Artifacts, and Recent Advances, Third Edition* 25–56 (2015).

51. Small angle x-ray scattering. (eds. Glatter, O. & Kratky, O.) (Academic Press, Inc., 1982).

52. Sethi, A. X-rays: Interaction with matter. in *Encyclopedia of Medical Devices and Instrumentation* (ed. Webster, J. G.) 590–599 (John Wiley & Sons, Inc., 2006). doi:10.1002/0471732877.emd263.

53. Bouxsein, M. L., Boyd, S. K., Christiansen, B. A., Guldberg, R. E., Jepsen, K. J. & Müller, R. Guidelines for assessment of bone microstructure in rodents using micro-computed tomography. *J. Bone Miner. Res.* 25, 1468–1486 (2010) doi:10.1002/jbmr.141.

54. Jacques, D. A. & Trewhella, J. Small-angle scattering for structural biology - Expanding the frontier while avoiding the pitfalls. *Protein Sci.* 19, 642–657 (2010) doi:10.1002/pro.351.

55. Hulmes, D. J. S., Miller, A., White, S. W. & Doyle, B. B. Interpretation of the meridional x-ray diffraction pattern from collagen fibers in terms of the known amino acid sequence. *Int. J. Biol. Macromol.* 2, 338–346 (1980).

56. White, S. W., Hulmes, D. J. S., Miller, A. & Timmins, P. A. Collagen-mineral axial relationship in calcified turkey leg tendon by X-ray and neutron diffraction. *Nature* 266, 421–425 (1977) doi:10.1038/266421a0.

57. Tengattini, A., Lenoir, N., Andò, E. & Viggiani, G. Neutron imaging for geomechanics: A review. *Geomech. Energy Environ.* 27, 100206 (2021) doi:10.1016/j.gete.2020.100206.

58. Tötzke, C., Kardjilov, N., Lenoir, N., Manke, I., Oswald, S. E. & Tengattini, A. What comes NeXT? – High-speed neutron tomography at ILL. *Opt. Express* 27, 28640 (2019) doi:10.1364/OE.27.028640.

59. Stavropoulou, E., Andò, E., Tengattini, A., Briffaut, M., Dufour, F., Atkins, D., *et al.* Liquid water uptake in unconfined Callovo Oxfordian clay-rock studied with neutron and X-ray imaging. *Acta Geotech.* 14, 19–33 (2019) doi:10.1007/s11440-018-0639-4.

60. Stavropoulou, E., Andò, E., Roubin, E., Lenoir, N., Tengattini, A., Briffaut, M., *et al.* Dynamics of water absorption in Callovo-Oxfordian claystone revealed with multimodal x-ray and neutron tomography. *Front. Earth Sci.* 8, 6 (2020) doi:10.3389/feart.2020.00006.

61. Lukić, B., Tengattini, A., Dufour, F. & Briffaut, M. Visualising water vapour condensation in cracked concrete with dynamic neutron radiography. *Mater. Lett.* 283, 128755 (2021) doi:10.1016/j.matlet.2020.128755.

62. Dauti, D., Tengattini, A., Dal Pont, S., Toropovs, N., Briffaut, M. & Weber, B. Analysis of moisture migration in concrete at high temperature through in-situ neutron tomography. *Cem. Concr. Res.* 111, 41–55 (2018) doi:10.1016/j.cemconres.2018.06.010.

63. Willmott, P. R. X-ray sources at large-scale facilities. in *Magnetism and Accelerator-Based Light Sources.* (eds. Bulou, H., Joly, L., Mariot, J. & Cheurer, F.) vol. 262 1–37 (Springer Proceedings in Physics, 2021). doi:10.1007/978-3-030-64623-3_1.

64. Kern, A. X-ray sources and optics. *International Tables for Crystallography Volume H: Powder diffraction* (eds. Gilmore, C. J., Kaduk, J. A. & Schenk, H.) vol. H (International Union of Crystallography, 2019). doi:10.1107/97809553602060000115.

65. Neutron scattering facilities in Europe - Present status and future perspectives Author: *ESFRI Scripta Volume I Neutron*.

66. Findlay, D. A practical guide to the ISIS neutron and muon source. (2021).

67. Neutron users in Europe: Facility-based insights and scientific trends. (2020).

68. HFIR: Providing unique capabilities for research and isotope production. (2019).

69. Austin, L., Kumar, R., Kousar, B., Lampadaris, C. H. & Lucas, M. M. MAX IV Laboratory. (2018) doi:10.13140/RG.2.2.18419.63527.

70. Hammouda, B. Probing nanoscale structures - the SANS toolbox. (National Institute of Standards and Technology, 2006).

71. Engström, A. & Finean, J. B. Low-angle x-ray diffraction of bone. *Nature* 171, 564–564 (1953) doi:10.1038/171564b0.

72. Le Cann, S., Törnquist, E., Silva Barreto, I., Fraulob, M., Albini Lomami,

H., Verezhak, M., *et al.* Spatio-temporal evolution of hydroxyapatite crystal thickness at the bone-implant interface. *Acta Biomater.* 116, 391–399 (2020) doi:10.1016/j.actbio.2020.09.021.

73. Grünewald, T. A., Liebi, M., Wittig, N. K., Johannes, A., Sikjaer, T., Rejnmark, L., *et al.* Mapping the 3D orientation of nanocrystals and nanostructures in human bone: Indications of novel structural features. *Sci. Adv.* 6, eaba4171 (2020) doi:10.1126/sciadv.aba4171.

74. Turunen, M. J., Lages, S., Labrador, A., Olsson, U., Tägil, M., Jurvelin, J. S., *et al.* Evaluation of composition and mineral structure of callus tissue in rat femoral fracture. *J. Biomed. Opt.* 19, 025003 (2014) doi:10.1117/1.JBO.19.2.025003.

75. Giannini, C., Siliqi, D., Ladisa, M., Altamura, D., Diaz, A., Beraudi, A., *et al.* Scanning SAXS-WAXS microscopy on osteoarthritis-affected bone - An age-related study. *J. Appl. Crystallogr.* 47, 110–117 (2014) doi:10.1107/S1600576713030215.

76. Bünger, M., Foss, M., Erlacher, K., Li, H., Zou, X., Langdahl, B., *et al.* Bone nanostructure near titanium and porous tantalum implants studied by scanning small angle x-ray scattering. *Eur. Cells Mater.* 12, 81–91 (2006) doi:10.22203/eCM.v012a10.

77. Gourrier, A., Li, C., Siegel, S., Paris, O., Roschger, P., Klaushofer, K., *et al.* Scanning small-angle X-ray scattering analysis of the size and organization of the mineral nanoparticles in fluorotic bone using a stack of cards model. *J. Appl. Crystallogr.* 43, 1385–1392 (2010) doi:10.1107/S0021889810035090.

78. Mathavan, N., Turunen, M. J., Tägil, M. & Isaksson, H. Characterising bone material composition and structure in the ovariectomized (OVX) rat model of osteoporosis. *Calcif. Tissue Int.* 97, 134–144 (2015) doi:10.1007/s00223-015-9991-7.

79. Choi, Y., Shin, E. J., Seong, B. S. & Paik, D. J. Application of small angle neutron scattering on the analysis of Korean compact jaw bone. *Met. Mater. Int.* 18, 895–898 (2012) doi:10.1007/s12540-012-5023-6.

80. Choi, Y., Paik, D. J., Bogdanov, S. G., Valiev, E. Z., Borisova, P. A., Murashev, M. M., *et al.* Neutron scattering on humane compact bone. *Phys. B Condens. Matter* 551, 218–221 (2018) doi:10.1016/j.physb.2018.01.020.

81. Feldkamp, L. A. A., Davis, I. C., Kress, J. W. W., Davis, L. C. & Kress, J. W. W. Practical cone-beam algorithm. *J. Opt. Soc. Am.* 1, 612–619 (1984).

82. Strobl, M., Manke, I., Kardjilov, N., Hilger, A., Dawson, M. & Banhart, J. Advances in neutron radiography and tomography. *J. Phys. D. Appl. Phys.* 42, 243001 (2009) doi:10.1088/0022-3727/42/24/243001.

83. Kampschulte, M., Langheinirch, A., Sender, J., Litzlbauer, H., Althöhn, U., Schwab, J., *et al.* Nano-computed tomography: Technique and applications. *RoFo* 188, 146–154 (2016) doi:10.1055/s-0041-106541.

84. Tengattini, A., Lenoir, N., Andò, E., Giroud, B., Atkins, D., Beaucour, J., *et al.* NeXT-Grenoble, the neutron and x-ray tomograph in Grenoble. *Nucl. Instruments Methods Phys. Res. Sect. A Accel. Spectrometers, Detect. Assoc. Equip.* 968, 163939 (2020) doi:10.1016/j.nima.2020.163939.

85. Trtik, P., Meyer, M., Wehmann, T., Tengattini, A., Atkins, D., Lehmann, E. H., *et al.* PSI 'Neutron Microscope' at ILL-D50 Beamline - First results. in *Materials Research Proceedings* vol. 15 23–28 (2020). doi:10.21741/9781644900574-4.

86. Bernhardt, R., Scharnweber, D., Müller, B., Thurner, P., Schliephake, H., Wyss, P., *et al.* Comparison of microfocus- and synchrotron x-ray tomography for the analysis of osteointegration around Ti6Al4V implants. *Eur. Cells Mater.* 7, 42–51 (2004) doi:10.22203/eCM.v007a05.

87. Schillinger, B. Estimation and measurement of l/d on a cold and thermal neutron guide. *Nondestruct. Test. Eval.* 16, 141–150 (2001) doi:10.1080/10589750108953071.

88. Hsieh, J. Image artifacts: Appearances, causes, and corrections. in *Computed Tomography, Second Edition* 207–299 (SPIE, 2015). doi:10.1117/3.817303.ch7.

89. Boas, F. E. & Fleischmann, D. CT artifacts: causes and reduction techniques. *Imaging Med.* 4, 229–240 (2012) doi:10.2217/iim.12.13.

90. Cormack, A. M. Reconstruction of densities from their projections, with applications in radiological physics. *Phys. Med. Biol.* 18, 003 (1973) doi:10.1088/0031-9155/18/2/003.

91. Ritman, E. L. Micro-computed tomography - Current status and developments. *Annu. Rev. Biomed. Eng.* 6, 185–208 (2004) doi:10.1146/annurev.bioeng.6.040803.140130.

92. Rydberg, J., Buckwalter, K. A., Caldemeyer, K. S., Phillips, M. D., Conces, D. J., Aisen, A. M., *et al.* Multisection CT: Scanning techniques and clinical applications. *RadioGraphics* 20, 1787–1806 (2000) doi:10.1148/radiographics.20.6.g00nv071787.

93. Müller, R. Hierarchical microimaging of bone structure and function. *Nat. Rev. Rheumatol.* 5, 373–381 (2009) doi:10.1038/nrrheum.2009.107.

94. Lespessailles, E., Chappard, C., Bonnet, N. & Benhamou, C. L. Imaging techniques for evaluating bone microarchitecture. *Jt. Bone Spine* 73, 254–261 (2006) doi:10.1016/j.jbspin.2005.12.002.

95. Neldam, C. A. & Pinholt, E. M. Synchrotron μCT imaging of bone,

titanium implants and bone substitutes - A systematic review of the literature. *J. Cranio-Maxillofacial Surg.* 42, 801–805 (2014) doi:10.1016/j.jcms.2013.11.015.

96. Palle, J., Wittig, N. K., Østergaard, M., Jensen, A. B. & Birkedal, H. The osteocyte lacuno-canalicular network in bone investigated by synchrotron radiation-based techniques. in *Developments in X-Ray Tomography XII* (eds. Müller, B. & Wang, G.) vol. 11113 39 (SPIE, 2019). doi:10.1117/12.2531980.

97. Bach-Gansmo, F. L., Weaver, J. C., Jensen, M. H., Leemreize, H., Mader, K. S., Stampanoni, M., *et al.* Osteocyte lacunar properties in rat cortical bone: Differences between lamellar and central bone. *J. Struct. Biol.* 191, 59–67 (2015) doi:10.1016/j.jsb.2015.05.005.

98. Fernández, M. P., Witte, F. & Tozzi, G. Applications of x-ray computed tomography for the evaluation of biomaterial-mediated bone regeneration in critical-sized defects. *J. Microsc.* 277, 179–196 (2020) doi:10.1111/jmi.12844.

99. Raina, D. B., Larsson, D., Sezgin, E. A., Isaksson, H., Tägil, M. & Lidgren, L. Biomodulation of an implant for enhanced bone-implant anchorage. *Acta Biomater.* 96, 619–630 (2019) doi:10.1016/j.actbio.2019.07.009.

100. Agholme, F., Li, X., Isaksson, H., Ke, H. Z. & Aspenberg, P. Sclerostin antibody treatment enhances metaphyseal bone healing in rats. *J. Bone Miner. Res.* 25, 2412–2418 (2010) doi:10.1002/jbmr.135.

101. Le Cann, S., Tudisco, E., Turunen, M. J., Patera, A., Mokso, R., Tägil, M., *et al.* Investigating the mechanical characteristics of bone-metal implant interface using in situ synchrotron tomographic imaging. *Front. Bioeng. Biotechnol.* 6, (2019) doi:10.3389/fbioe.2018.00208.

102. Thorfve, A., Palmquist, A. & Grandfield, K. Three-dimensional analytical techniques for evaluation of osseointegrated titanium implants. *Mater. Sci. Technol.* 31, 174–179 (2015) doi:10.1179/1743284714Y.0000000687.

103. Kazakia, G. J., Burghardt, A. J., Cheung, S. & Majumdar, S. Assessment of bone tissue mineralization by conventional x-ray microcomputed tomography: Comparison with synchrotron radiation microcomputed tomography and ash measurements. *Med. Phys.* 35, 3170–3179 (2008) doi:10.1118/1.2924210.

104. Grassi, L. & Isaksson, H. Extracting accurate strain measurements in bone mechanics: A critical review of current methods. *J. Mech. Behav. Biomed. Mater.* 50, 43–54 (2015) doi:10.1016/j.jmbbm.2015.06.006.

105. Turunen, M. J., Le Cann, S., Tudisco, E., Lovric, G., Patera, A., Hall, S. A., *et al.* Sub-trabecular strain evolution in human trabecular bone. *Sci. Rep.* 10, 13788 (2020) doi:10.1038/s41598-020-69850-x.

106. Zanolli, C., Schillinger, B., Beaudet, A., Kullmer, O., Macchiarelli, R., Mancini, L., *et al.* Exploring hominin and non-hominin primate dental fossil remains with neutron microtomography. *Phys. Procedia* 88, 109–115 (2017) doi:10.1016/j.phpro.2017.06.014.

107. Mays, C., Bevitt, J. & Stilwell, J. Pushing the limits of neutron tomography in palaeontology: Three-dimensional modelling of in situ resin within fossil plants. *Palaeontol. Electron.* 1–12 (2017) doi:10.26879/808.

108. Laaß, M. & Schillinger, B. Reconstructing the auditory apparatus of therapsids by means of neutron tomography. *Phys. Procedia* 69, 628–635 (2015) doi:10.1016/j.phpro.2015.07.089.

109. Pugliesi, R., Pereira, M. A. S., Andrade, M. L. G., Basso, J. M. L., Voltani, C. G. & Gonzales, I. C. Study of the fish fossil Notelops brama from Araripe-Basin Brazil by neutron tomography. *Nucl. Instruments Methods Phys. Res. Sect. A Accel. Spectrometers, Detect. Assoc. Equip.* 919, 68–72 (2019) doi:10.1016/j.nima.2018.12.001.

110. Zanolli, C., Schillinger, B., Kullmer, O., Schrenk, F., Kelley, J., Rössner, G. E., *et al.* When x-rays do Not work. Characterizing the internal structure of fossil hominid dentognathic remains using high-resolution neutron microtomographic imaging. *Front. Ecol. Evol.* 8, (2020) doi:10.3389/fevo.2020.00042.

111. Schwarz, D., Vontobel, P., Lehmann, E. H., Meyer, C. a & Bongartz, G. Neutron tomography of internal structures of vertebrate remains: A comparison with x-ray computed tomography. *Palaeontol. Electron.* 8, 30A:11p (2005).

112. Urciuoli, A., Zanolli, C., Fortuny, J., Almécija, S., Schillinger, B., Moyà-Solà, S., *et al.* Neutron-based computed microtomography: Pliobates cataloniae and Barberapithecus huerzeleri as a test-case study. *Am. J. Phys. Anthropol.* 166, 987–993 (2018) doi:10.1002/ajpa.23467.

113. Schillinger, B., Beaudet, A., Fedrigo, A., Grazzi, F., Kullmer, O., Laaß, M., *et al.* Neutron imaging in cultural heritage research at the FRM II reactor of the Heinz Maier-Leibnitz Center. *J. Imaging* 4, 22 (2018) doi:10.3390/jimaging4010022.

114. Fedrigo, A., Strobl, M., Williams, A. R., Lefmann, K., Lindelof, P. E., Jørgensen, L., *et al.* Neutron imaging study of 'pattern-welded' swords from the Viking Age. *Archaeol. Anthropol. Sci.* 10, 1249–1263 (2018) doi:10.1007/s12520-016-0454-5.

115. Roubin, E., Andò, E. & Roux, S. The colours of concrete as seen by x-rays and neutrons. *Cem. Concr. Compos.* 104, 103336 (2019) doi:10.1016/j.cemconcomp.2019.103336.

116. Tudisco, E., Jailin, C., Mendoza, A., Tengattini, A., Andò, E., Hall, S. A.,

*et al.* An extension of digital volume correlation for multimodality image registration. *Meas. Sci. Technol.* 28, 095401 (2017) doi:10.1088/1361-6501/aa7b48.

117. Fedrigo, A., Marstal, K., Bender Koch, C., Andersen Dahl, V., Bjorholm Dahl, A., Lyksborg, M., *et al.* Investigation of a Monturaqui impactite by means of bi-modal x-ray and neutron tomography. *J. Imaging* 4, 72 (2018) doi:10.3390/jimaging4050072.

118. Peruzzi, N., Galli, S., Helmholz, H., Kardjilov, N., Krüger, D., Markötter, H., *et al.* Multimodal ex vivo methods reveal that Gd-rich corrosion byproducts remain at the implant site of biodegradable Mg-Gd screws. *Acta Biomater.* (2021) doi:10.1016/j.actbio.2021.09.047.

119. Reilly, D. T., Burstein, A. H. & Frankel, V. H. The elastic modulus for bone. *J. Biomech.* 7, 271–275 (1974) doi:10.1016/0021-9290(74)90018-9.

120. Reilly, D. T. & Burstein, A. H. The elastic and ultimate properties of compact bone tissue. *J. Biomech.* 8, 393–405 (1975) doi:10.1016/0021-9290(75)90075-5.

121. Currey, J. & Hernandez, C. J. Chapter A1 - Cortical bone, Chapter A2 - Cancellous bone. in *Handbook of Biomaterial Properties* (eds. Murphy, W., Black, J. & Hastings, G.) 3–22 (Springer New York, 2016). doi:10.1007/978-1-4939-3305-1.

122. Dhoble, A., Padole, P. & Dhoble, M. Bone mechanical properties: A brief review. *Trends Biomater. Artif. Organs* 26, 25–30 (2012).

123. Morgan, E. F., Unnikrisnan, G. U. & Hussein, A. I. Bone mechanical properties in healthy and diseased states. *Annu. Rev. Biomed. Eng.* 20, 119–143 (2018) doi:10.1146/annurev-bioeng-062117-121139.

124. Wu, D., Isaksson, P., Ferguson, S. J. & Persson, C. Young's modulus of trabecular bone at the tissue level: A review. *Acta Biomater.* 78, 1–12 (2018) doi:10.1016/j.actbio.2018.08.001.

125. Carter, D. R. & Spengler, D. M. Mechanical properties and composition of cortical bone. *Clin. Orthop. Relat. Res.* NA;, 192???217 (1978) doi:10.1097/00003086-197809000-00041.

126. Schwarcz, H. P., Abueidda, D. & Jasiuk, I. The ultrastructure of bone and its relevance to mechanical properties. *Front. Phys.* 5, (2017) doi:10.3389/fphy.2017.00039.

127. Endo, K., Yamada, S., Todoh, M., Takahata, M., Iwasaki, N. & Tadano, S. Structural strength of cancellous specimens from bovine femur under cyclic compression. *PeerJ* 4, e1562 (2016) doi:10.7717/peerj.1562.

128. Morgan, E. F., Bayraktar, H. H. & Keaveny, T. M. Trabecular bone modulus-density relationships depend on anatomic site. *J. Biomech.* 36, 897–904 (2003) doi:10.1016/S0021-9290(03)00071-X.

129. Wall, A. & Board, T. The compressive behavior of bone as a two-phase porous structure. in *Classic Papers in Orthopaedics* vol. 59 457–460 (Springer London, 2014). doi:10.1007/978-1-4471-5451-8_116.

130. Ang, B. L. S., Tan, Y. J., Ng, Y. J. P., Ong, S. H. F., Yap, S. Y., Gwee, S. X., *et al.* The Effect of specimen geometry on the mechanical behavior of trabecular bone specimens. *Solid State Phenom.* 185, 129–132 (2012) doi:10.4028/www.scientific.net/SSP.185.129.

131. Halgrin, J., Chaari, F. & Markiewicz, É. On the effect of marrow in the mechanical behavior and crush response of trabecular bone. *J. Mech. Behav. Biomed. Mater.* 5, 231–237 (2012) doi:10.1016/j.jmbbm.2011.09.003.

132. Maquer, G., Musy, S. N., Wandel, J., Gross, T. & Zysset, P. K. Bone volume fraction and fabric anisotropy are better determinants of trabecular bone stiffness than other morphological variables. *J. Bone Miner. Res.* 30, 1000–1008 (2015) doi:10.1002/jbmr.2437.

133. Matsuura, M., Eckstein, F., Lochmüller, E.-M. & Zysset, P. K. The role of fabric in the quasi-static compressive mechanical properties of human trabecular bone from various anatomical locations. *Biomech. Model. Mechanobiol.* 7, 27–42 (2008) doi:10.1007/s10237-006-0073-7.

134. Hölzer, A., Pietschmann, M. F., Rösl, C., Hentschel, M., Betz, O., Matsuura, M., *et al.* The interrelation of trabecular microstructural parameters of the greater tubercle measured for different species. *J. Orthop. Res.* 30, 429–434 (2012) doi:10.1002/jor.21525.

135. Bindl, R., Oheim, R., Pogoda, P., Beil, F. T., Gruchenberg, K., Reitmaier, S., *et al.* Metaphyseal fracture healing in a sheep model of low turnover osteoporosis induced by hypothalamic-pituitary disconnection (HPD). *J. Orthop. Res.* 31, 1851–1857 (2013) doi:10.1002/jor.22416.

136. Manda, K., Xie, S., Wallace, R. J., Levrero-Florencio, F. & Pankaj, P. Linear viscoelasticity - bone volume fraction relationships of bovine trabecular bone. *Biomech. Model. Mechanobiol.* 15, 1631–1640 (2016) doi:10.1007/s10237-016-0787-0.

137. Chih-Ling, L. A study of human and bovine trabecular bones using nanoindentation and quantitative backscattered electron imaging. (The University of Queensland, 2016). doi:10.14264/uql.2016.164.

138. Wang, B., Chen, R., Chen, F., Dong, J., Wu, Z., Wang, H., *et al.* Effects of moisture content and loading profile on changing properties of bone micro-biomechanical characteristics. *Med. Sci. Monit.* 24, 2252–2258 (2018) doi:10.12659/MSM.906910.

139. Broz, J. J., Simske, S. J., Greenberg, A. R. & Luttges, M. W. Effects of rehydration state on the flexural properties of whole mouse long bones. *J. Biomech. Eng.* 115, 447–449 (1993) doi:10.1115/1.2895510.

140. Lievers, W. B., Poljsak, A. S., Waldman, S. D. & Pilkey, A. K. Effects of dehydration-induced structural and material changes on the apparent modulus of cancellous bone. *Med. Eng. Phys.* 32, 921–925 (2010) doi:10.1016/j.medengphy.2010.06.001.

141. Currey, J. D. The effects of drying and re-wetting on some mechanical properties of cortical bone. *J. Biomech.* 21, 439–441 (1988) doi:10.1016/0021-9290(88)90150-9.

142. Bunk, O., Bech, M., Jensen, T. H., Feidenhans'l, R., Binderup, T., Menzel, A., *et al.* Multimodal x-ray scatter imaging. *New J. Phys.* 11, 123016 (2009) doi:10.1088/1367-2630/11/12/123016.

143. Kraft, P., Bergamaschi, A., Broennimann, C., Dinapoli, R., Eikenberry, E. F., Henrich, B., *et al.* Performance of single-photon-counting PILATUS detector modules. *J. Synchrotron Radiat.* 16, 368–375 (2009) doi:10.1107/S0909049509009911.

144. Lindner, P. & Schweins, R. The D11 small-angle scattering instrument: A new benchmark for SANS. *Neutron News* 21, 15–18 (2010) doi:10.1080/10448631003697985.

145. Richard, D. ., Ferrand, M. . & Kearley, G. J. Analysis and visualisation of neutron-scattering data. *J. Neutron Res.* 4, 33–39 (1996) doi:10.1080/10238169608200065.

146. Allen, A. J., Zhang, F., Kline, R. J., Guthrie, W. F. & Ilavsky, J. NIST standard reference material 3600: Absolute intensity calibration standard for small-angle x-ray scattering. *J. Appl. Crystallogr.* 50, 462–474 (2017) doi:10.1107/S1600576717001972.

147. Turunen, M. J., Khayyeri, H., Guizar-Sicairos, M. & Isaksson, H. Effects of tissue fixation and dehydration on tendon collagen nanostructure. *J. Struct. Biol.* 199, 209–215 (2017) doi:10.1016/j.jsb.2017.07.009.

148. Schneider, C. A., Rasband, W. S. & Eliceiri, K. W. NIH Image to ImageJ: 25 years of image analysis. *Nat. Methods* 9, 671–675 (2012) doi:10.1038/nmeth.2089.

149. Doube, M., Kłosowski, M. M., Arganda-Carreras, I., Cordelières, F. P., Dougherty, R. P., Jackson, J. S., *et al.* BoneJ: Free and extensible bone image analysis in ImageJ. *Bone* 47, 1076–1079 (2010) doi:10.1016/j.bone.2010.08.023.

150. Püspöki, Z., Storath, M., Sage, D. & Unser, M. Transforms and operators for directional bioimage analysis: A survey. in *Focus on Bio-Image Informatics* 69–93 (Springer, 2016). doi:10.1007/978-3-319-28549-8_3.

151. Stamati, O., Andò, E., Roubin, E., Cailletaud, R., Wiebicke, M., Pinzon, G., *et al.* spam: Software for practical analysis of materials. *J. Open Source Softw.* 5, 2286 (2020) doi:10.21105/joss.02286.

152. Masic, A., Bertinetti, L., Schuetz, R., Chang, S.-W., Metzger, T. H., Buehler, M. J., *et al.* Osmotic pressure induced tensile forces in tendon collagen. *Nat. Commun.* 6, 5942 (2015) doi:10.1038/ncomms6942.

153. Nyman, J. S., Roy, A., Shen, X., Acuna, R. L., Tyler, J. H. & Wang, X. The influence of water removal on the strength and toughness of cortical bone. *J. Biomech.* 39, 931–938 (2006) doi:10.1016/j.jbiomech.2005.01.012.

154. Agarwal, R., González-García, C., Torstrick, B., Guldberg, R. E., Salmerón-Sánchez, M. & García, A. J. Simple coating with fibronectin fragment enhances stainless steel screw osseointegration in healthy and osteoporotic rats. *Biomaterials* 63, 137–145 (2015) doi:10.1016/j.biomaterials.2015.06.025.

155. Forghani, R., De Man, B. & Gupta, R. Dual-energy computed tomography: Physical principles, approaches to scanning, usage, and implementation: Part 1. *Neuroimaging Clin. N. Am.* 27, 371–384 (2017) doi:10.1016/j.nic.2017.03.002.

156. Rajiah, P., Sundaram, M. & Subhas, N. Dual-energy CT in musculoskeletal imaging: What is the role beyond gout? *Am. J. Roentgenol.* 213, 493–505 (2019) doi:10.2214/AJR.19.21095.

157. Schock, J., Liebl, S., Achterhold, K. & Pfeiffer, F. Obtaining the spacing factor of microporous concrete using high-resolution Dual Energy X-ray Micro CT. *Cem. Concr. Res.* 89, 200–205 (2016) doi:10.1016/j.cemconres.2016.08.008.

158. Martins de Souza e Silva, J., Utsch, J., Kimm, M. A., Allner, S., Epple, M. F., Achterhold, K., *et al.* Dual-energy micro-CT for quantifying the time-course and staining characteristics of ex-vivo animal organs treated with iodine- and gadolinium-based contrast agents. *Sci. Rep.* 7, 17387 (2017) doi:10.1038/s41598-017-17064-z.

159. Xia, X., Hu, X., Mu, Y. & Zou, J. Dual-energy micro-CT using GAGG:Ce and LYSO:Ce scintillators. *IEEE Trans. Nucl. Sci.* 68, 236–244 (2021) doi:10.1109/TNS.2020.3048353.

# 9. Appended papers

I. Mineralization of cortical bone during maturation and growth in rabbits

II. Comparison of small-angle neutron and x-ray scattering for studying cortical bone nanostructure

III. Dual modality neutron and x-ray tomography for enhanced image analysis of the bone-metal interface

IV. Hydration state affects neutron tomographic images of bone